Constitutive activation of the PI3K-Akt-mTORC1 pathway sustains the m.3243A>G mtDNA mutation

Chih-Yao Chung[1], Kritarth Singh[1], Vassilios N Kotiadis[1], Gabriel E Valdebenito[1], Jee Hwan Ahn[1], Emilie Topley[1], Joycelyn Tan[1], William D Andrews[1], Benoit Bilanges[2], Robert D S Pitceathly[3], Gyorgy Szabadkai[1,4,5], Mariia Yuneva[5], Michael R Duchen[1,6,*]

1 Department of Cell and Developmental Biology and Consortium for Mitochondrial Research, UCL, Gower Street, London WC1E 6BT, UK

2 UCL Cancer Institute, 72 Huntley St, London WC1E 6DD, UK

3 Department of Neuromuscular Diseases, UCL Queen Square Institute of Neurology and The National Hospital for Neurology and Neurosurgery, Queen Square, London WC1N 3BG, UK

4 Department of Biomedical Sciences, University of Padua, via G. Colombo 3, 35100, Padua, Italy

5 The Francis Crick Institute, 1 Midland Rd, London NW1 1AT, UK

6 Lead Contact

*Correspondence: m.duchen@ucl.ac.uk

Keywords: mitochondria; mtDNA; mtDNA mutations; nutrient signalling; m.3243A>G; PI3K; Akt; mTORC1; mitophagy

ABSTRACT

Mutations of the mitochondrial genome (mtDNA) cause a range of profoundly debilitating clinical conditions for which treatment options are very limited. Most mtDNA diseases show heteroplasmy – tissues express both wild-type and mutant mtDNA. While the level of heteroplasmy broadly correlates with disease severity, the relationships between specific mtDNA mutations, heteroplasmy, disease phenotype and severity are poorly understood. We have carried out extensive bioenergetic, metabolomic and RNAseq studies on heteroplasmic patient derived cells carrying the most prevalent disease related mtDNA mutation, m.3243A>G. These studies reveal that the mutation promotes changes in metabolites which is associated with the upregulation of the PI3K-Akt-mTORC1 axis in patient-derived cells and tissues. Remarkably, pharmacological inhibition of PI3K, Akt, or mTORC1 activated mitophagy, reduced mtDNA mutant load and rescued cellular bioenergetic function. The rescue was prevented by inhibition of mitophagy. The PI3K-Akt-mTORC1 axis thus represents a

30 potential therapeutic target that may benefit people suffering from the consequences of the
31 m.3243A>G mutation.

32

33 **INTRODUCTION**

34 Mitochondria control cellular bioenergetic homeostasis and serve as a hub for cell metabolism and
35 cell signalling pathways. Human mitochondria contain a circular plasmid-like DNA (mtDNA) which
36 encodes 13 proteins which act as subunits of the electron transport chain (ETC) and 24 RNAs essential
37 for mitochondrial protein synthesis. Mutations of mtDNA affect around 1 in 5000 of the population[1]
38 and cause a range of diseases for which no effective treatment is available[2,3]. Over half of the known
39 pathogenic mutations are found within tRNA genes, in which the m.3243A>G mutation, a $tRNA^{Leu}$
40 point mutation accounts for about 40% of adult patients of primary mitochondrial diseases[1,4].
41 Clinically, signs and symptoms in patients with mtDNA mutations are highly heterogeneous[2,5]. The
42 tissues primarily affected vary depending on the specific mtDNA mutations, and our understanding of
43 the relationships between mtDNA mutations, disease phenotype and severity is very limited[2,3]. The
44 majority of diseases caused by mutations of mtDNA are heteroplasmic – tissues express both normal
45 and mutation carrying mtDNA. This is a confounding complication, as disease expression may differ
46 radically between patients with the same mutation but with different mutant load. While disease
47 severity broadly correlates positively with the relative burden of mutant mtDNA, we know remarkably
48 little about the determinants of the mutant mtDNA burden[3,6–8].

49 Mitochondrial quality control pathways, including mitophagy, mitochondrial biogenesis pathways and
50 mitochondrial shaping mechanisms, are critically involved in regulating mitochondrial energy
51 homeostasis[9,10]. Several studies have demonstrated the accumulation of damaged mitochondria and
52 defective mitophagy as a hallmark of mtDNA diseases and age-related neurodegeneration, suggesting
53 that the presence of pathogenic mtDNA alone is not sufficient to drive selection against the mutation
54 by the activation of mitophagy[11–15]. We therefore asked how cell signalling pathways influence these
55 pathways in the disease model, as adaptive - or maladaptive – responses to impaired oxidative
56 phosphorylation (OxPhos) and changes in intermediary metabolism, and whether these pathways play
57 a role as determinants of mutant load and disease severity.

58 In this study, we have characterised the metabolic phenotype of patient-derived cells bearing the
59 m.3243A>G ($tRNA^{Leu}$) mutation. This is the most common heteroplasmic mtDNA mutation[1,4], and,
60 clinically, is expressed variably but may include diabetes, sensorineural deafness, myopathy,
61 encephalopathy, lactic acidosis and stroke-like episodes (MELAS). We have found that the basal
62 expression and activity of the PI3K-Akt-mTORC1 pathway were increased in the mutant cells, and were

strongly associated with redox imbalance, oxidative stress, and glucose dependence. Phosphorylation of Akt and ribosomal protein S6 (a downstream target of mTORC1) were increased in muscle biopsies from other patients with the mutation, confirming that this signalling pathway is constitutively activated in patient tissues. Remarkably, inhibition of PI3K, Akt, or mTORC1 all substantially reduced mutant load and rescued mitochondrial bioenergetic function. This process is mediated by the upregulation of mitophagy which is absolutely required for rescue of mitochondrial function and reduction in mutant load. These findings thus reveal that in response to the m.3243A>G mutation, metabolism is rewired, and activity of the PI3K-Akt-mTORC1 axis is increased, presumably as an adaptive response to metabolic changes driven by the mutation. The finding that inhibition of the pathway reduces mutant load and rescues mitochondrial bioenergetic function suggests that activation of this signalling pathway is, in fact, maladaptive, that activation of the pathway sustains disease progression and that pharmacological intervention in this signalling pathway represents a potential therapeutic strategy in patients with these dreadful diseases.

RESULTS

The m.3243A>G mutation causes mitochondrial dysfunction and glucose dependence, resulting in redox imbalance and oxidative stress.

To explore the metabolic and cell signalling impact of the m.3243A>G mutation, we used six cell lines: fibroblasts derived from two patients carrying the mutation, two controls matched for age and gender, an A549 cybrid cell line carrying the mutation and its Wild-type (WT) counterpart. PCR-RFLP[16] was used to ensure the presence of the m.3243A>G mutation and ARMS-qPCR[17] was used to quantify the m.3243A>G mutation load in these cell models. One patient-derived line (henceforth referred to as patient 1) showed a mutant load of 86.2 ± 2.3%; a second line (referred to as patient 2) showed a mutant load of 30.3 ± 3.5%, and the mutant load was 79.0 ± 0.3% in the cybrid cells (Fig. 1A; for more details about the patients please see Methods).

To characterise the metabolic phenotype of the mutant cells, respiratory rate was measured using the Seahorse XFe96 extracellular flux analyser. These measurements showed a profound decrease in resting respiratory rate, ATP dependent respiration and in maximal respiratory capacity and an increase in extracellular acidification rate (ECAR) in both patient lines (Fig. 1B). Consistent with these findings, immunoblotting of respiratory chain supercomplexes using blue native gel electrophoresis (BNGE), which identifies non-denatured macromolecular assemblies, revealed disrupted expression of respiratory chain proteins in the mutant cells (Fig. 1C). Notably, there was a very large decrease in assembly of supercomplexes I_2+ III_2 +IV_n, III_2+IV_1 and III_2/IV_2 and in complex IV_1. Surprisingly, levels of complex II, which is entirely encoded by nuclear genes, were also consistently and significantly reduced in all mutant cell lines. Mitochondrial membrane potential ($\Delta\psi_m$) was reduced in both patient-derived fibroblast lines (Fig. 1D). The decrease in $\Delta\psi_m$ was greater in cells from patient 1 than from patient 2, consistent with the greater mutant load in patient 1.

Mitochondrial dysfunction may alter rates of free radical generation by the respiratory chain. The rate of increase of dihydroethidium (DHE) fluorescence (Fig. S1A), reflecting the intracellular rate of production of reactive oxygen species (ROS), was significantly increased both in patient fibroblasts compared to matched controls (Fig. 1Ei). MitoSOX, a mitochondria-targeted form of DHE, revealed a significant increase in the rate of ROS generation in the mitochondria in the mutant cells (Fig. 1Eii), suggesting that the increased rate of ROS generation is likely the consequence of an impaired respiratory chain. Together, the m.3243A>G mutation results in mitochondrial dysfunction and elevated ROS generation.

We wondered whether glucose or glutamine metabolism is altered in the mutant cells, supporting cellular bioenergetic homeostasis and compensating for the mitochondrial dysfunction. Using time-

109 lapse live-cell imaging, we quantified cell growth rates by fitting the curves of cell confluence with an
110 exponential cell growth model (Fig. S1B) under a variety of nutrient conditions. Growth rates were
111 significantly reduced in all mutant fibroblasts compared to their control counterparts (Fig. S1C).
112 Moreover, the cell proliferation rate was significantly reduced in all mutant cells in 1 and 5 mM glucose
113 media (Fig. 1F) but not in low concentrations of glutamine, suggesting that the patient-derived cells
114 are significantly more dependent on glucose metabolism. Consistently, the rate of uptake of the
115 fluorescent glucose analogue, 2-NBDG, was significantly increased in patient fibroblasts compared to
116 controls (Fig. 1G).

117 The cytosolic NADH:NAD^+ ratio is a function of glycolytic flux (which consumes NAD^+, generating
118 NADH), lactate production through lactate dehydrogenase (LDH) which produces lactate and
119 regenerates NAD^+ from NADH and the activity of malate/aspartate and the glycerol phosphate
120 shuttles that exchange NADH and NAD^+ between cytosol and mitochondrial matrix. We used the
121 genetically encoded reporter SoNar[18] to quantify the cytosolic NADH:NAD^+ ratio (Fig. S1D). The basal
122 NADH:NAD^+ ratio was significantly increased in the patient fibroblasts compared to controls,
123 consistent with increased regeneration of NADH through LDH activity (Fig 1H). Addition of exogenous
124 pyruvate can either support mitochondrial activity, increasing OxPhos, or stimulate LDH activity to
125 generate lactate, changing the cytosolic NADH:NAD^+ ratio. In control cells, pyruvate addition
126 decreased the cytosolic NADH:NAD^+ ratio, but had no significant effect on the high NADH:NAD+ ratio
127 in the mutant cells (Fig. 1H), suggesting that in the latter, LDH flux is already saturated. These data are
128 also consistent with significantly higher levels of lactate produced by the patient fibroblasts compared
129 to controls (Fig. 1I). The pH of the growth media, reflecting cellular lactate production, was also
130 measured using the absorbance of the pH indicator, phenol red. The acidification of media by mutant
131 cells was significantly greater than that of controls (Fig S1E). These data recapitulate the lactic acidosis
132 which is characteristic of patients with the m.3243A>G mutation[19]**,** and suggest that in patient
133 fibroblasts, increased activity of LDH may compensate for the decreased regeneration of NAD^+ by
134 mitochondria, supporting increased glycolytic flux. Of note, these metabolic features were
135 recapitulated in the A549 cybrid cells (Fig S1C, F-L), including cell growth rate, OCR (since OCR is
136 affected by cellular mitochondrial content, its value was normalised to their increased mtDNA copy
137 number, Fig. S1F), ECAR, $\Delta\psi_m$, ROS generation, glucose uptake, glucose dependence, the cytosolic
138 NADH:NAD^+ ratio. Together, these data confirm that glucose uptake and glucose catabolism into
139 lactate are upregulated and cytosolic NADH:NAD^+ ratio is increased in the mutant cells.

140

141 **The m.3243A>G mutation remodels glucose metabolism towards increased lipid biosynthesis.**

142 To investigate the glucose-dependent metabolic alterations in the mutant cells and identify metabolic
143 signals which might drive changes in cell signalling, glucose uniformly labelled with isotopic carbon
144 ([U-^{13}C]-glucose) was used to trace its metabolic fate in the cells by gas chromatography-mass
145 spectrometry (GC-MS). The pattern and abundance of ^{13}C enrichment in downstream metabolites
146 were used to determine the relative contribution of glucose into different metabolic pathways. First,
147 partial least squares discriminant analysis (PLS-DA) for the concentration of metabolites (Fig. 2A)
148 showed a clear separation between patient fibroblasts and controls (Fig. S2A). The analysis of
149 metabolic pathways revealed enrichment of glycerolipid metabolism, pentose phosphate pathway
150 (PPP), glycolysis, the tricarboxylic acid (TCA) cycle and aspartate metabolism (Fig. S2B). Tracing the
151 fate of ^{13}C-glucose through glycolysis (Fig. 2B), we found that the enrichment of ^{13}C in glucose-6-
152 phosphate (G6P) in the patient fibroblasts was at a similar level as in controls, but the total pools of
153 G6P were increased (Fig. 2A) consistent with increased glucose uptake. Although the end products of
154 glycolysis, intracellular pools of pyruvate and lactate in the patient fibroblasts, were maintained at
155 similar levels with controls in terms of ^{13}C enrichments and concentrations (Fig. 2A and 2B), the levels
156 and the ^{13}C enrichment of glycerol-3-phosphate (αG3P) were increased. The latter suggests the
157 increased activity of glycerol-3-phosphate dehydrogenase in response to increased cytosolic
158 NADH:NAD$^+$ ratio, which may drive elevated lipid biosynthesis. Interestingly, while the absolute
159 concentrations of alanine were increased in the mutant cells, its ^{13}C enrichment was decreased,
160 suggesting a contribution from other nutrient sources. Similarly, the total concentration of serine was
161 increased in patient fibroblasts, despite decreased synthesis of serine from glucose, suggesting
162 increased serine uptake from extracellular media (Fig. 2A, 2B and S2C).

163 Consistent with OxPhos defects, levels of the TCA cycle intermediates, malate, fumarate and succinate
164 were decreased in the mutant cells (Fig. 2A). Interestingly, the enrichment of m+3 isotopologues of
165 these TCA cycle intermediates and aspartate were significantly increased in the patient fibroblasts
166 (Fig. 2B). To enter the TCA cycle, glucose-derived pyruvate is converted into acetyl-CoA by pyruvate
167 dehydrogenase (PDH). In this case the catabolism of [U-^{13}C]-glucose results in m+2 enrichment of TCA
168 cycle intermediates, including oxaloacetate (OAA), a precursor of aspartate. In contrast, m+3
169 isotopologues of TCA cycle intermediates are generated if pyruvate is converted into OAA by pyruvate
170 carboxylase (PC). Immunoblotting for PC and phospho-PDH expression revealed elevated PC
171 expression in both patient fibroblasts and cybrid cells and increased levels of phosphorylated PDH
172 (indicating its reduced activity) in patient 2 fibroblasts and cybrid cells (Fig. S2D). As the glucose
173 contribution into the TCA cycle is usually low in conventional cell culture systems, this slight but
174 significant difference in the enrichment of ^{13}C is meaningful. The switch from PDH to PC as means of
175 channelling glucose-derived carbon into the TCA cycle in mutant fibroblasts is consistent with the

176 increased NADH:NAD+ ratio, which stimulates the activity of pyruvate dehydrogenase kinase,
177 phosphorylating PDH and inhibiting its activity. Our findings from the stable-isotope-labelling
178 approach and comparative metabolomics thus reveal a profound remodelling of glucose metabolism
179 as a consequence of OxPhos defects arising from the m.3243A>G mutation.

180

181 **Chronic activation of the PI3K-Akt-mTORC1 axis in the m.3243A>G mutant cells impairs autophagic**
182 **flux and mitochondrial degradation via mitophagy**

183 The metabolic phenotype shown above points to reprogramming of nutrient-sensing signalling
184 networks in the m.3243A>G mutant cells. We therefore carried out an RNA sequencing screen to
185 examine global changes in the expression profiles of the patient fibroblasts (Fig. S3A). Using a
186 significance level of false discovery rate (FDR) < 0.05, we identified 3394 transcripts of which 1849
187 were upregulated and 1545 were downregulated (Fig. S3B). A multi-dimensional principal component
188 analysis also confirmed good accordance between biological triplicates as well as close clustering of
189 transcripts from patient fibroblasts (Fig. S3C). The enrichment analysis identified 'mitochondrial
190 dysfunction', 'TCA cycle' as the altered metabolic pathways in patient fibroblasts (Fig. S3D). Analysis
191 of individual genes involved in these pathways showed a general downregulation of OxPhos genes
192 (Fig. S3E). Specifically, the increased expression of PC was consistent with the immunoblotting data
193 (Fig. S2D) and correlated with altered TCA cycle activity (Fig. S3F). The enhancement of glycolytic flux
194 in the mutant cells reported by the metabolomic data was supported by the increased expression of
195 hexokinase 1 (HK1). A general decrease of enzymes in serine/glycine metabolism (Fig. S3G) and an
196 altered expression of amino acid transporters (Fig. S3H) also matched our observation of increased
197 serine in the metabolomics measurements. These findings further validated the metabolic footprint
198 observed in patient-derived cells from the metabolomic studies.

199 Consistent with the above results, the network analysis of these differentially expressed genes
200 identified the strong enrichment of PI3K-Akt and mTOR pathways in patient fibroblasts (Fig. 3A and
201 Fig. S3I; Table S1). We therefore validated these data at the protein expression level. Immunoblotting
202 confirmed increased phosphorylation of Akt (S473) relative to total Akt, as well as phosphorylation of
203 the downstream mTORC1 target S6 ribosomal protein in patient fibroblasts (Fig. 3B) and the cybrid
204 cells (Fig. S3J). While control fibroblasts showed a growth factor-dependent activation of Akt in
205 response to increased serum concentration in growth media, phospho-Akt was elevated in patient
206 cells even when growth factors were low (1% FBS) and increased only slightly in response to an
207 elevated serum concentration. Similarly, the patient fibroblasts exhibited increased mTORC1
208 activation independently of the serum concentration, revealed by increased phospho-S6 levels. PI3K-

209 Akt-mTORC1 signalling also antagonizes the activity of the cellular energy sensor, AMP-activated
210 protein kinase (AMPK) and suppresses macromolecular catabolism by autophagy. We therefore
211 measured AMPK phosphorylation in response to different serum concentration by immunoblotting,
212 but found no significant difference between patient and control fibroblasts. We further measured
213 phosphorylation of the Akt substrates, p-TSC2 (S939) and p-PRAS40 (T246), and the mTORC1
214 substrate, p-4EBP1 (S65), of patient fibroblasts grown in 10% or 1% FBS media. In all of these,
215 phosphorylation was increased in cells carrying the mtDNA mutation independent of serum
216 concentration, again consistent with constitutive activation of the pathway in the mutant cells
217 (Fig.S3K). These results suggest that the constitutive induction of PI3K-Akt-mTORC1 signalling
218 remodels cell metabolism, independently of growth factor stimulation.

219 To establish that the PI3K-Akt-mTORC1 axis is also constitutively active in patients with the
220 m.3243A>G mtDNA mutation, we measured p-Akt/Akt and p-S6/S6 by immunofluorescence in a
221 muscle biopsy from a patient with an 82% mutant load of the m.3243A>G mutation causing MELAS,
222 (not one of the donors used to obtain the fibroblasts; matched H&E and COX staining are shown in
223 Fig. S4A). These data confirmed a significant increase in p-Akt and p-S6 in the muscle biopsy, which
224 argues that upregulation of this pathway is a clinical feature of the disease and not a function of the
225 cultured cells (Fig. 3C-D). Re-analysis of a published RNA-seq data set[22] from muscle biopsies of MELAS
226 patients also confirmed the activation of PI3K-Akt-mTORC1 signalling in patients (Table S4). In
227 summary, activation of the PI3K-Akt-mTORC1 axis is a common feature of m.3243A>G mutation both
228 in vivo and in vitro.

229 Analysis of the differentially expressed genes in patient fibroblasts also identified autophagy and
230 unfolded protein response as the enriched cellular process in patient fibroblasts (Fig. 3Ei; Table S2-
231 S3). We therefore explored the impact of chronic induction of PI3K-Akt-mTORC1 signalling on
232 autophagic flux in the mutant cells (Fig. S4Bi)[13,20]. The mRNA expression of genes involved in
233 autophagy was highly altered in patient fibroblasts (Fig S4Bii). We next monitored LC3B turnover in
234 the presence and absence of chloroquine (CQ) or Bafilomycin A1 (Baf A1), both of which prevent
235 lysosomal acidification and inhibit function, using LC3B immunoblotting as a readout. The mutant cells
236 showed an increased conversion to LC3BI to the lipidated LC3BII form (autophagosome) but the
237 difference in LC3BII accumulation in the presence of CQ was not significantly different between control
238 and mutant cells (Fig. 3Eii-iii), indicating a defect in the late stage of autophagosome to autolysosome
239 conversion/fusion in the mutant cells. We also measured the autophagic flux using a mCherry-EGFP-
240 LC3B tandem reporter[21] by live-cell imaging, in which the EGFP is quenched in an acidic environment,
241 seen as red puncta. Consistent with the above result, the ratio of green/red puncta was low in control
242 compared to patient cells, representing the formation of mature autolysosomes and a high autophagy

243 flux. In contrast, the ratio of green/red puncta and both the number and size of double-positive puncta
244 were increased in mutant cells, indicating impaired autophagosome maturation into autolysosomes
245 (Fig. 3F). These features, LC3B turnover and autophagic flux, were recapitulated in patient fibroblasts
246 treated with Baf A1 (Fig. S4C) and in the A549 cybrid cells treated with CQ or Baf A1 (Fig S4D-F).
247 Altogether, these results confirm that autophagic flux is impaired in the mutant cells and further
248 indicate that an autophagy imbalance may contribute to metabolic and proteostatic stress in the
249 mutant cells as a consequence of the activation of PI3K-Akt-mTORC1.

250 Given the impaired mitochondrial form and function and autophagy imbalance observed in
251 m.3243A>G mutant cells, we sought to examine the mitochondrial quality control by mitophagy
252 pathway. Similar to mCherry-EGFP-LC3B, we used COX8-EGFP-mCherry (EGFP-mCherry targeted to
253 mitochondrial matrix) as a mitophagy reporter in cybrid cells. The proportion of mitophagic positive
254 cells was quantified by a flow cytometry-based approach in which an arbitrary threshold of red
255 fluorescence was used to indicate the mitophagic polulation. The flow cytometry data revealed an
256 increase in mitophagic population in response to oligomycin and antimycin A (Oligo+AA)-induced
257 mitophagy, which was completely abolished when the control cells were co-treated with Baf A1.
258 However, the mitophagic population in cybrid cell did not alter significantly when treated with either
259 Oligo+AA or Oligo+AA+Baf A1 suggesting an accumulation of autophagosomes-containing
260 mitochondria or its impaired maturation (Fig. S4G). To visualise the delivery of impaired mitochondria
261 to lysosomes, we transfected the fibroblasts with mitochondrial-targeted mKeima (mt-Keima), which
262 undergoes a shift in excitation spectrum within acidic lysosomes indicating the conversion of
263 autophagosome to autolysosomes. A ratio of signal excited at 543nm and 458nm (F_{543}/F_{458}) provides
264 a quantitative readout of mitophagic activity. The control fibroblasts exhibited punctate structures
265 showing strong mt-Keima signal at 543 nm which indicated that a subpopulation of mitochondria was
266 delivered to lysosomes. Quantification of the ratio image also demonstrated a high ratio (F_{543}/F_{458})
267 signal corresponding to increased formation of autolysosomes containing degraded mitochondria. In
268 contrast, the patient fibroblasts exhibited fragmented mitochondrial network throughout the
269 cytoplasm displaying a strong fluorescence at 458 nm but a diminished mt-Keima signal at 543 nm.
270 The subpopulation of mitochondria with high ratio (F_{543}/F_{458}) signal was significantly decreased which
271 suggested a defect in autolysosome maturation in patient fibroblasts (Fig. 3G-H). Altogether these
272 findings indicate that chronic activation of PI3K-Akt-mTORC1 signalling impairs mitophagy pathway
273 which may lead to accumulation of damaged mitochondria in m.3243A>G mutant cell.

274

275 **Pharmacological inhibition of PI3K-Akt-mTORC1 signalling reduces mutant load, rescues**
276 **mitochondria function and lowers glucose dependence in the m.3243A>G mutant cells**

277 At this point, we asked what the functional consequences of the activation of the PI3K-Akt-mTORC1
278 axis are and whether it represents an adaptation to impaired OxPhos. We therefore systematically
279 inhibited each component of the axis in turn using well-established pharmacological inhibitors (Fig.
280 4A)[20] and explored the consequences for mutant mtDNA burden and the pathophysiological and
281 biochemical features that we have described above.

282 These inhibitors include two inhibitors of class 1 PI3K, LY294002 (LY, 5 μM) and GDC0941 (GDC, 1 μM),
283 an inhibitor of Akt, MK2206 (MK, 1 μM) and an inhibitor of mTORC1, rapamycin (RP, 5 μM). In both
284 the fibroblasts from patient 1 and the cybrid cells, treatment with LY, GDC, MK, or RP, led to a striking
285 and progressive decrease in mutant mtDNA load over 6-12 weeks of sustained treatment in which the
286 mutant load fell from ~80% to values as low as 40% (Fig. 4Bi-ii). Interestingly, in the absence of the
287 inhibitors, the fibroblasts from patient 2 showed a progressive increase in mutant load with time in
288 culture, rising from ~30% to around 70% over 3 months (Fig. 4Biii). Treatment with any of the inhibitors
289 significantly suppressed the rate of increase in mutant load decreasing the total change by around
290 20%. Although the decrease in mutant load took many weeks to develop, changes in protein
291 phosphorylation state were evident within a day of starting treatment (Fig. S5A-C). Accordingly,
292 inhibition of PI3K by LY or GDC or inhibition of Akt by MK2206 reduced Akt and mTOR phosphorylation,
293 while rapamycin inhibited mTOR phosphorylation but had no impact on Akt. None of the treatments
294 had any immediate effect on AMPK phosphorylation. However, AMPK activity gradually increased at
295 later time points after drug treatments, suggesting an induction of catabolic processes such as
296 autophagy and improvement in sensing the bioenergetic status of the m.3243A>G mutant cells[23].

297 To investigate whether the decrease in mutant load after drug treatment was reflected by a
298 concomitant change in mitochondrial function, we measured the mitochondrial bioenergetic status
299 and the metabolic phenotype of the patient-derived cells. Mitochondrial membrane potential of the
300 cells treated with RP or LY showed a complete recovery to levels that were not significantly different
301 from control cells (Fig. 4C). Although $\Delta\psi_m$ of the cells treated with GDC or MK was higher than the
302 mutant cells, it was still slightly but significantly lower than controls. Similarly, measurements of
303 mitochondrial respiration showed that both basal (50-65% of controls) and maximal respiratory
304 capacity (69-86% of controls) were increased in cells treated with any of the inhibitors (Fig. 4D). Of
305 note, the rescue of mitochondrial bioenergetics by these inhibitors was recapitulated in the A549
306 cybrid cells (Fig S5D-E).

307 We then focused on RP and LY, the two most potent inhibitors, for further experiments. The
308 improvement in mitochondrial respiration suggested a metabolic shift towards OxPhos.
309 Measurements of cytosolic redox state using SoNar (Fig. 4E and S5F) showed a significant reduction in
310 basal NADH:NAD^+ ratio and increased response to pyruvate addition in the long-term treated patient-
311 derived cells, implying a decreased glycolytic flux. Measurements of glucose and lactate
312 concentrations in the media showed a profound decrease in lactate secretion following LY and RP
313 treatments (Fig 4F). The patient fibroblasts were also cultured in media containing glucose or
314 galactose as a primary carbon source to further assess their dependence on glycolysis. LY- and RP-
315 treated cells, but not mutant controls, grew well in the galactose media, indicating a reduced glycolytic
316 dependence after the drug treatments (Fig. 4G). Also, the mutant cells showed an increased
317 supercomplex assembly as well as rescue of individual components of the mitochondrial ETC following
318 all drug treatments (Fig. 4H). These changes were accompanied by a decrease in the rates of ROS
319 production in cells treated with LY and RP (Fig. 4I). These changes in cell metabolism were again
320 recapitulated in the A549 cybrid cells (Fig S5F-I).

321 Altogether, these data demonstrate that the long-term treatment of the mutant cells with inhibitors
322 of the PI3K-Akt-mTORC1 axis reduces mutant load and reverses the biochemical consequences of the
323 mutation, rescuing mitochondrial function, reducing glucose dependence and lactate secretion. These
324 data strongly argue that the chronic constitutive activation of the PI3K-Akt-mTORC1 axis serves as a
325 maladaptive response in this disease model and helps to sustain the mtDNA mutant load.

326

327 **Reduction of the m.3243A>G mutant load by inhibition of the PI3K-Akt-mTORC1 axis is cell-**
328 **autonomous**

329 The chronic activation of the PI3K-Akt-mTORC1 axis and increased mutant load have deleterious
330 effects on cellular function and amplify the pathophysiological consequences of the mutation.
331 However, this raises questions about the underlying mechanism by which inhibition of the axis reduces
332 mutant load and rescues mitochondrial function. A possible explanation for the response to drug
333 treatments is that inhibition of the signalling pathway may promote the selective growth of cell
334 populations with low mutant load or selective elimination of cells with high mutant loads. We
335 therefore carried out long term measurements of growth rates and cell death (Fig. 5Ai-ii). Cells were
336 pre-treated with either vehicle, LY, or RP for the time periods as specified in Fig. 5B (pretreatment)
337 and then seeded into 96-well plates for measuring cell growth rate and cell death with either vehicle,
338 LY, or RP (treatment). Although treatment with either LY or RP significantly slowed cell proliferation
339 in both fibroblast and cybrid cells at the time point of 0-week pretreatment (Fig. 5B, upper panel), the

340 changes were small. The cell growth rate was stable in cybrid cells treated with LY or RP, suggesting
341 that there was no clonal expansion. In fibroblasts, growth rates of cells were not altered by LY but
342 increased by RP after 4-week pretreatment. However, the growth rate of patient 1 fibroblasts was not
343 further increased by RP after 8-week pretreatment. In contrast, a significant decrease of mutation
344 load was clearly established after 4 weeks of treatment, suggesting that the change of mutation load
345 is independent of the rate of cell growth. On the other hand, cell death in the drug-treated groups
346 were even lower than in the mutant controls, suggesting that the drug treatments were beneficial,
347 and there was no selective killing of mutant cells (Fig. 5B, lower panel). Treating the cybrid cells with
348 GDC or MK showed similar results in terms of cell growth and death (Fig. S6A-B).

349 To determine definitively whether the reduction of mutant load in response to the drug treatments is
350 cell-autonomous, we used a PCR-based technique, TaqMan SNP genotyping, at single cell resolution
351 to measure the distributions of the m.3243A>G heteroplasmy in a cell population (Fig. 5Aiii). The
352 TaqMan technique was first validated by measuring the mutation loads of a population of cells and
353 then to establish the range of single cell mutant load across the population (Fig. S6C). The distribution
354 of mutant load in the cybrid cells ranged from 50-80%, showing a Gaussian distribution (Fig. S6D).
355 Although we found that this technique is less accurate than ARMS-qPCR and tends to overestimate
356 the mutant load when it is lower than 50% and underestimate the mutant load when it is higher than
357 50%, the average single cell mutant load was consistent with that of the whole cell population,
358 suggesting a good precision of the technique. Measurement of the relative m.3243A>G heteroplasmy
359 in patient fibroblasts and cybrid cells following treatment with LY and RP for 6 and 12 weeks
360 respectively showed a frequency distribution which clearly segregated the treated group as a distinct
361 population from the untreated group (Figs. 5C-D). The distribution of the mutant load in treated
362 groups shifted to significantly lower levels compared to the untreated group.

363 To determine whether the reduction in the m.3243A>G mutant load is phenocopied at the protein
364 expression level, we immunostained the mtDNA-encoded cytochrome c oxidase I (MT-COI) in patient
365 1 fibroblasts. The presence of 7 UUA-encoded leucine residues within MT-COI renders the m.3243A>G
366 $tRNA^{Leu(UUR)}$ cells prone to codon-specific translational defect[24]. Immunofluorescence staining revealed
367 a significant decrease in MT-COI expression in patient 1 fibroblasts compared to controls (Fig. S6E).
368 Following drug treatments, these cells showed a partial but significant recovery of MT-COI expression.
369 The single cell analysis of MT-COI expression segregated the drug-treated and untreated groups in a
370 distribution pattern similar to the m.3243A>G mtDNA distribution shown in Fig. 5D. A diminished
371 expression of MT-COI also correlated with the reduced assembly and activity of supercomplexes
372 shown in Fig. 4H. Together, these results strongly suggest that rather than the enrichment of a specific

373 cell population, the reduction in m.3243A>G mtDNA mutant load caused by inhibition of PI3K-Akt-
374 mTORC1 signalling operates across the whole population and is cell-autonomous.

375

376 **Restoration of autophagic/mitophagic flux by PI3K-Akt-mTORC1 inhibition is necessary to reduce**
377 **the m.3243A>G mutant load.**

378 The data from the single cell analysis strongly argue that the change in mutant load is a cell-
379 autonomous phenomenon. We then asked what mechanisms select against the mutant mtDNA. A
380 possible explanation could be the elimination of the mutant mtDNA by reducing the total mtDNA copy
381 number while amplifying the dominant mtDNA, resembling 'the bottleneck' effect – the selection
382 mechanism of mtDNA in the germline or embryo[4,6]. We therefore quantified the total mtDNA copy
383 number of the drug-treated cells at a series of time points, but found no significant changes between
384 the mutant control and drug-treated cells (Fig. S7A) and the total mtDNA copy number remained
385 stable across the duration of drug treatments.

386 It also seemed plausible that the removal of dysfunctional mitochondria via mitophagy may reduce
387 the mutant load in cells with the mtDNA mutation[25,26]. Indeed, long-term treatment with LY or RP all
388 significantly increased the conversion and accumulation of LC3BII (autophagosome) in the presence
389 of CQ compared to untreated cells (Fig. 6A). Notably, the autophagic flux, evident by a high
390 LC3BII/LC3BI ratio in the presence of CQ, increased progressively with time closely mirroring the rate
391 of decrease in mutant load (see Fig. 4B). Measurement of autophagic flux using the mCherry-GFP-LC3
392 probe showed a significant increase in the formation of autolysosomes (red puncta) as early as 24 h
393 of drug treatment and increased upon long-term treatment in patient fibroblasts (Fig. 6B). Moreover,
394 the ratio of green/red puncta numbers decreased significantly, suggesting the restoration of
395 autophagic flux in the m.3243A>G mutant cells after drug treatment. Moreover, similarly results were
396 also found in the cybrid cells and the mutant cells treated with GDC or MK (Fig. S7B-E). Of note, analysis
397 of the cybrid cells transfected with mCherry-GFP-LC3 by flow cytometry also showed an increase in
398 cells with low GFP intensity after RP or LY treatment (Fig S7D).

399 To evaluate how the increased efficacy of autophagy affects specific status of mitophagy, the cybrid
400 cells were transfected with COX8-mCherry-EGFP, as a reporter of mitophagy. The long-term drug
401 treatment with RP and LY dramatically increased the proportion of cells with low GFP intensity,
402 suggesting the restoration of mitophagy flux (Fig. S7F). Similarly, after 24 h of drug treatments in
403 patient fibroblasts transfected with mt-Keima (Fig. 6C), the (F_{543}/F_{458}) ratio increased significantly with
404 an increase in red puncta (degraded mitochondria). Altogether, these findings confirm that inhibition

405 of PI3K-Akt-mTORC1 signalling restores autophagy and promotes mitophagic flux in the m.3243A>G
406 mutant cells.

407 The progressive decrease in mutant load and increase in autophagic flux with time following PI3K-Akt-
408 mTORC1 inhibition in the m.3243A>G mutant cells strengthened the idea that upregulated mitophagic
409 flux drives selection against the mutant mtDNA and decreases the mutant load. To explore this further,
410 we quantified mitophagy in patient fibroblasts expressing mt-Keima, cotreated with CQ in
411 combination with RP or LY. The cotreatment with CQ reversed the effect of LY and RP on mitophagy,
412 decreasing the high ratio (F_{543}/F_{458}) signal to levels comparable to untreated patient fibroblasts (Fig.
413 6C and S7G). Remarkably, CQ treatment over 6 weeks in the patient fibroblasts and cybrid cells
414 completely prevented the decrease of mutant load in response to PI3K-Akt-mTORC1 inhibition (Fig.
415 6D), demonstrating that increased mitophagy is necessary to reduce the burden of mutant mtDNA.
416 This also argues strongly that the reduction in mutant load must be a cell-autonomous effect and
417 cannot be attributed to the selective growth of subpopulations of the cells. To confirm the
418 mechanisms are specific to the m.3243A>G mutation, we also examined the effects of LY and RP in
419 cells carrying another heteroplasmic mtDNA point mutation – the m.8993T>G – generated by the
420 Minczuk lab[27]. In these cells, there is no difference in the phosphorylation of Akt and S6 and
421 autophagic flux assessed by LC3B (Fig. S7Hi). Furthermore, inhibition of the PI3K-Akt-mTORC1 axis had
422 no impact on mutant load (Fig. S7Hii), suggesting that hyperactivation of the PI3K-Akt-mTORC1 axis is
423 relatively disease specific. Together, effective autophagy/mitophagy triggered by inhibition of the
424 PI3K-Akt-mTORC1 axis is necessary to eliminate the mutant m.3243A>G mtDNA.

425 **DISCUSSION**

426 The clinical presentation of diseases caused by pathogenic mtDNA mutations is highly
427 heterogeneous[4–6]. The association between specific mtDNA mutations, heteroplasmic mutant load,
428 disease manifestation and severity are poorly understood. In the present study, we have
429 systematically characterised the metabolic and cell signalling phenotype of cells bearing the
430 m.3243A>G mutation, the most prevalent mtDNA mutation, which is responsible for mitochondrial
431 encephalomyopathy, lactic acidosis and stroke like episodes (MELAS) or Maternally inherited Diabetes
432 and Deafness (MIDD) and related disorders. We found that the changes in metabolism were
433 associated with the constitutive hyperactivation of the PI3K-Akt-mTORC1 pathway specifically to the
434 m.3243A>G mtDNA mutation. Most notably, pharmacological inhibition of PI3K, Akt, or mTORC1 in
435 the patient-derived cells reduced mutant load and rescued mitochondrial bioenergetic function. These
436 inhibitors promoted mitophagy, which was absolutely required to mediate the effects of these
437 treatments (Fig. 6E). In contrast to the m.3243A>G mtDNA variant, previous studies have reported
438 downregulation of Akt activity in cells carrying the m.8993T>G mutation[28], in which inhibition of the
439 PI3K-Akt-mTORC1 pathway had no impact on mutant load or mitochondrial function (Fig. S7H). These
440 findings suggest that the changes in signalling pathways are disease specific and may represent a link
441 between genotype and phenotype.

442 Metabolic features of the patient fibroblasts and cybrid cells are consistent with most of the previous
443 studies of the m.3243A>G mutation, including mitochondrial dysfunction, upregulated glycolysis,
444 increased ROS production, and redox imbalance[5,15,19,23,24,29]. However, metabolic profiling of cells
445 bearing the mutation is limited in the literature. Metabolomics data showed that reductive
446 carboxylation of glutamine is a major mechanism to support cell survival and maintain redox balance
447 in the m.8993T>G mutation cell models[27,30]. In contrast, using a similar approach, we found that
448 glucose anabolism (i.e. upregulated upper glycolysis, PPP, and lipid synthesis) is increased in the
449 m.3243A>G mutant cells and these cells are dependent on glucose for cell survival and proliferation.
450 Also, increased TCA cycle entry of pyruvate through PC, which, combined with the prediction of
451 enriched malate-aspartate shuttle pathway (Fig. S2B) may serve as a mechanism to maintain cellular
452 $NADH:NAD^+$ balance to support glycolytic flux and promote antioxidant capacity[27,31]. This difference in
453 metabolism between the m.8993T>G and m.3243A>G mutations argues that the mtDNA mutations
454 cannot be seen as one disease[32,33]. Thus, the rewired metabolism specific to the m.3243A>G mutation
455 drew our attention to the corresponding changes in cell signalling.

456 The alterations of metabolism in the m.3243A>G mutant cells strongly imply a perturbation in cell
457 signalling, especially implicating the PI3K-Akt-mTORC1 pathway, which has been widely studied in

458 cancer signalling and metabolism[34]. For example, oxidative stress and redox imbalance may activate
459 PI3K-Akt, the increased glycolytic flux and PPP implies an activated Akt-NRF2 signalling, the increased
460 PC expression and p-PDH suggests an accumulation of acetyl-CoA associated with Akt-mTORC1
461 activity[34]. Metabolic pathway analysis using RNA-seq data recapitulated these metabolic changes in
462 the patient fibroblasts. Moreover, network analysis using the RNA-seq data further validated the link
463 between the metabolic changes and altered cell signalling in cells carrying the m.3243A>G mutation.

464 Indeed, the network analysis also identified EIF2 (eukaryotic initiation factor 2) and PTEN
465 (phosphatase and tensin homolog) signalling as the top downregulated pathways (Fig. 3A). PTEN is a
466 negative regulator of the PI3K-Akt-mTORC1 axis. Although the mechanisms of crosstalk between PI3K-
467 Akt-mTORC1 and EIF2 pathways are still unclear, these two pathways seem to communicate and
468 determine cell fate under stress[35,36]. Of note, IPA upstream analysis showed an upregulation of
469 transcription factors in the EIF2 pathway – ATF4 and DDIT3 (CHOP) (Table S3-4). ATF4 acts as a
470 prototypical downstream target coupling mitochondrial proteotoxic stress to the activation of ISR
471 (integrated stress response)[37] and derives remodelling of one-carbon metabolism (serine/glycine and
472 folate metabolism)[38]. Although we observed an increase of serine concentration in fibroblasts bearing
473 the m.3243A>G mutation, incorporation of ^{13}C-glucose into serine was reduced. Also, expression of
474 genes related to serine/glycine metabolism was generally reduced (see Fig. S3G). These data imply
475 that in fibroblasts carrying the m.3243A>G mutation, unlike 'Deletor' mice[38], serine metabolism is
476 downregulated. On the other hand, given that the UPR^{mt} (mitochondrial unfolded protein response)
477 maintaining mutant mtDNA in a *C. elegans* model is mitopahgy independent[39], exploring the role of
478 ISR/UPR^{mt} in the maintenance of the m.3243A>G mutation and disease progression by suppressing
479 eIF2α phosphorylation will be interesting. Furthermore, in a published RNA-seq data set of muscle
480 biopsies from patients with MELAS [22], FGF21 (~48 fold) and GDF15 (~9 fold) were upregulated,
481 matching previous findings reported from muscle tissue of 'Deletor' mice[38]. In contrast, in the present
482 study, while we did not find changes in these two genes in the patient fibroblasts, we did find
483 upregulation of FGF16 (~33 fold), suggesting that changes in FGF pathways in response to
484 mitochondrial dysfunction might be tissue specific.

485 Previous studies have suggested that different levels of heteroplasmy of the m.3243A>G mutation in
486 cybrid cells result in different gene expression patterns and even in discrete changes in
487 metabolism[40,41]. Another study showed that JNK (c-Jun N-terminal kinases) was activated by ROS in
488 cybrid m.3243A>G cells, further reducing RXRA (retinoid X receptor alpha) expression[42]. In contrast,
489 our data did not show inhibition of the RXRA pathway and suggest that chronic activation of the PI3K-
490 Akt-mTORC1 pathway is a general response in cells with the m.3243A>G mutation despite very
491 different levels of mutant load. Remarkably, we found that prolonged treatment with inhibitors of

492 each component of the PI3K-Akt-mTORC1 axis reliably and reproducibly reduced mutant burden and
493 rescued mitochondrial function in the mutant cells. Although inhibition of PI3K-Akt-mTORC1 axis has
494 been shown to be beneficial in several mitochondrial and neurological disease models, the underlying
495 mechanisms remain elusive [13,20,43–45]. As a result, the therapeutic efficacy of the inhibition may be
496 distinct and limited in different models. A study of a mouse model of Leigh syndrome showed that
497 rapamycin, while delaying the progression of the disease, failed to improve OxPhos[46]. Similarly,
498 another study showed that mTORC1 inhibition failed to improve either mitochondrial bioenergetics
499 or survival in a mouse model of mitochondrial encephalomyopathy (Coq9^{R239X})[47]. Our data from cells
500 with the m.8993T>G mutation suggest that changes in signalling pathways may differ between mtDNA
501 diseases, perhaps pointing towards the mechanisms that define differences in disease phenotype
502 between different mitochondrial diseases, and emphasising that therapeutic options should be
503 considered separately for each disease related to mtDNA mutations. However, since both the PI3K-
504 Akt-mTORC1 axis and the accumulation of mtDNA mutations have been associated with
505 neurodegeneration, ageing and cancers, our study may implicate in a broader biomedical
506 context[4,6,9,20,34].

507 Overall, the m.3243A>G mutation causes a profound cell metabolic and signalling remodelling,
508 although the causality between the observed alterations in metabolism and cell signalling of the
509 m.3243A>G mutant cells is not yet conclusive. Our working model is that activation of the PI3K-Akt-
510 mTORC1 pathway drives a metabolic rewiring of the cell, redirecting glycolytic metabolism and
511 promoting lactate production. Activating the pathway suppresses mitophagy, allowing the mutation
512 to propagate and thus maintaining the mutant load. Inhibition of the PI3K-Akt-mTORC1 axis promotes
513 mitophagy, reduces mutant load and improves bioenergetic competence in a cell-autonomous way.
514 Thus, we propose that nutrient-sensing pathways that may have evolved as adaptive responses to
515 altered cellular metabolism prove to be maladaptive, driving a positive feedback cycle that may shape
516 the phenotype of the disease and determine disease progression. In conclusion, our results suggest
517 that activation of the PI3K-Akt-mTORC1 axis by changes in intermediary metabolism controls the
518 heteroplasmic burden of the m.3243A>G mutation and may define disease progression and severity
519 in a cell-autonomous manner. These data strongly suggest that cell signalling pathways activated by
520 altered metabolism represent potential therapeutic targets that may benefit people suffering from
521 diseases caused by mtDNA mutations.

522 **FIGURE LEGENDS**

523 **Figure 1. The m.3243A>G mtDNA mutation causes mitochondrial dysfunction and switches cell**
524 **metabolism to a more glycolytic phenotype, resulting in redox imbalance and oxidative stress.**

525 (A) PCR-RFLP and ARMS-qPCR were used to quantify the mutation load for patient-derived fibroblasts
526 (n = 3 independent biological samples) and A549 cybrid cells (n = 5 independent biological samples).

527 (B) Cell respiratory capacity was measured using the Seahorse XFe96 extracellular flux analyser in
528 patient fibroblasts (n = 6 culture wells) showing a major decrease in oxygen consumption under all
529 conditions (i). Oxygen consumption dependent on ATP production (ii) – the response to oligomycin –
530 and extracellular acidification rate (ECAR) are plotted (iii).

531 (C) The expression of respiratory chain proteins and supercomplex assembly in patient fibroblasts
532 were assessed using blue native gels electrophoresis (BNGE, i) and quantified (ii), showing a major
533 decrease in the assembly of all supercomplexes from the patient-derived cells (n = 3 independent
534 experiments)

535 (D) The mitochondrial membrane potential of fibroblasts was measured using TMRM with confocal
536 microscopy (i) and quantified (ii), showing a significant decrease in potential (n = 5 independent
537 experiments). Scale bar = 50 μm.

538 (E) ROS production rates of patient fibroblasts were measured using the reporters, DHE (i) and
539 MitoSOX (ii). Rates of production were significantly increased in patient-derived cells (n = 6
540 independent biological samples).

541 (F) The growth rates of patient fibroblasts were measured under a range of different nutrient
542 conditions (normalised to the growth rate of each cell line in regular cell media), showing a decrease
543 of growth rate compared to controls at glucose concentrations of 5 and 1 mM (i) but not at low
544 glutamine (ii) concentrations (n = 6 culture wells for all conditions, 3 independent experiments).

545 (G) Glucose uptake in patient fibroblasts was measured using the fluorescent glucose analogue, 2-
546 NBDG, showing a significantly increased rate of glucose uptake in the patient fibroblasts (n = 14 culture
547 wells).

548 (H) $NADH:NAD^+$ ratio of fibroblasts was measured using the reporter, SoNar, under basal conditions
549 and after addition of pyruvate (200 μM, 30 min; i) and quantified (ii; n = 50 ± 10 cells). Scale bar = 100
550 μm.

551 (I) Lactate production (normalized to glucose consumption) was measured in the media of fibroblasts
552 using CuBiAn and showed a significant increase in lactate release in the media of patient-derived cells
553 (n = 4 independent biological samples).

554 All data are represented as mean ± S.D. and data were analysed by one-way ANOVA with Tukey's
555 multiple comparisons test (* $p < 0.05$, ** $p < 0.01$, *** $p < 0.001$, **** $p < 0.0001$).

556

557 **Figure S1. The metabolic phenotype of A549 cybrid cells recapitulates the metabolic features of**
558 **patient fibroblasts.**

559 (A) Rates of ROS production in A549 cybrid cells and the parental cells were measured using
560 dihydroethidium (DHE), as the rate of increase in red fluorescence intensity over 80 min incubation
561 with DHE.

562 (B-C) A scheme describing how growth rates were obtained by fitting growth curves with an
563 exponential cell growth model (B). (C) Based on the model, growth rate of fibroblasts (i, n = 3 culture
564 wells) and A549 cybrid cells cultured with regular medium were obtained (ii, n = 5 culture wells, p =
565 0.84).

566 (D) Schematic depicting the ratiometric probe for NADH:NAD^+, SoNar.

567 (E) pH in the media from patient fibroblasts cultured for 2 days was measured based on the ratiometric
568 property of the pH indicator, phenol red, in media and showing a lower pH in the media of patient
569 fibroblasts than that of controls (n = 6 independent biological samples).

570 (F) Mitochondrial DNA copy number of fibroblasts (i) and A549 cybrid cells (ii, n = 5 independent bio
571 logical samples).

572 (G) Cell respiratory capacity was also measured using the Seahorse XFe96 extracellular flux analyser
573 in A549 cybrid cells (n = 8 culture wells, further normalised to mtDNA copy number) showing a major
574 decrease in oxygen consumption under all conditions. Oxygen consumption dependent on ATP
575 production (ii) and ECAR are plotted (iii).

576 (H) The mitochondrial membrane potential of A549 cybrid cells measured using TMRM with confocal
577 imaging (i) and quantified (ii, n = 7 independent biological samples). Sale bar = 20 μm.

578 (I) ROS production rates of A549 cybrid cells reported by DHE (i, n = 9 independent biological samples)
579 and MitoSOX (ii, n = 3 independent biological samples).

580 (J) Glucose uptake in A549 cybrid cells was measured by 2-NBDG, showing a significantly increased
581 rate of glucose uptake in the cybrid cells compared to A549 controls (n = 21 culture wells).

582 (K) Cell growth rates of A549 cybrid cells were measured under a range of different nutrient conditions
583 (normalised to the growth rate of each cell line in regular cell media), showing a decreased rate of
584 growth of A549 cybrid cells compared to controls at glucose concentrations of 5 and 1 mM (i; n = 10
585 culture wells) but not at low glutamine concentrations (ii, n = 6 culture wells).

586 (L) $NADH:NAD^+$ ratio of A549 cybrid cells under basal condition and after addition of pyruvate (200
587 μM, 30 min; i) was measured by the probe and quantified (ii; n > 180 cells). Scale bar = 100 μm.

588 All data are represented as mean ± S.D. and were analysed by one-way ANOVA with Tukey's multiple
589 comparisons test for fibroblasts and by unpaired t test for cybrid cells (* $p < 0.05$, ** $p < 0.01$, *** $p <$
590 0.001, **** $p < 0.0001$).

591

592 **Figure 2. The m.3243A>G mutation rewires glucose metabolism towards increased anabolic**
593 **biosynthesis.**

594 (A) The heatmap of metabolite concentrations obtained by GC-MS was generated by MetaboAnalyst
595 5.0 (n = 3 technical replicates), revealing significant differences in the concentrations of several
596 metabolites between controls and patient fibroblasts.

597 (B) Schematic of simplified glucose metabolism of the cells (i) Red arrows, upregulated pathways or
598 reactions; three yellow circles of pyruvate and beyond, pyruvate is converted to OAA by pyruvate
599 carboxylase; three or two grey circles of pyruvate and beyond, pyruvate is converted to acetyl-CoA by
600 PDH. Tracing the distribution and abundance of ^{13}C enrichment in the intermediates of glycolysis (ii-
601 vi) and the TCA cycle (vii-xi) combined with Fig 2A and S2B revealed an increase in lipid synthesis and
602 PC activity (n = 3 independent biological samples).

603 All data, except Fig. 2A, are represented as mean ± S.D. and were analysed by one/two-way ANOVA
604 with Tukey's multiple comparisons test for fibroblasts (* $p < 0.05$, ** $p < 0.01$, *** $p < 0.001$, **** $p <$
605 0.0001).

606

607 **Figure S2. The metabolomic of fibroblasts carrying the m.3243A>G mutation are distinct from that**
608 **of their matched controls.**

609 (A) PLS-DA for the dataset of Fig. 2A showed that the metabolic profiles of patient fibroblasts were
610 distinct from that of controls.

611 (B) The concentration of metabolites obtained by GC-MS was used to determine the enriched
612 metabolic pathways in patient fibroblasts by MetaboAnalyst 5.0., suggesting that phospholipid
613 biosynthesis, PPP, glycolysis, TCA cycle, etc. were enriched (n = 6 technical replicates).

614 (C) With an increase of serine and alanine concentration (Fig 2A) in the patient cells, the incorporation
615 of ^{13}C into serine (i) and glycine (ii) were reduced, while alanine (iii) was not altered (mean ± S.D, of n
616 = 3 independent biological samples).

617 (D) Immunoblotting (i) of the expression of pyruvate carboxylase and phosphorylation state of PDH
618 showed an increase of pyruvate carboxylase expression and increased phosphorylation of PDH (S293)
619 in patient fibroblasts (ii) and A549 cybrid cells (iii) (n = 3 independent experiments for all cell lines).

620 All data, except Figs. S2A and S2B, are represented as mean ± S.D. and were analysed by one-way
621 ANOVA with Tukey's multiple comparisons test for fibroblasts and by unpaired t test for cybrid cells
622 (* $p < 0.05$, ** $p < 0.01$, *** $p < 0.001$, **** $p < 0.0001$)

623

624 **Figure 3. The PI3K-Akt-mTORC1 axis is upregulated in the m.3243A>G mutant cells, perturbing**
625 **autophagy and mitophagy.**

626 (A) Analysis of RNA-seq data from the patient fibroblasts by QIAGEN Ingenuity Pathway Analysis (IPA)
627 showed cell signalling pathways which are enriched in cells carrying the m.3243A>G mutation. These
628 include striking and significant increases in expression of pathways involving PI3K-Akt, mTOR, EIF2,
629 and NRF2. It is notable also that PTEN expression, a negative regulator of PI3K-Akt-mTOR signalling
630 was downregulated ($p < 0.05$).

631 (B) Immunoblotting of p-Akt (S473)/Akt, p-S6 (S235/236)/S6 and p-AMPK (T172)/AMPK in patient
632 fibroblasts grown in the presence of 10% or 1% FBS media (i), showing a major increase in p-Akt/Akt
633 (ii) and p-S6/S6 (iii) in the presence of 1% FBS media in the mutant cells. In contrast, there is no
634 difference in p-AMPK/AMPK (iv) (mean ± S.D. of n = 3 independent experiments).

635 (C-D) Immunofluorescence staining for p-Akt (S473)/Akt (Ci, n > 60 muscle fibres) and p-S6
636 (S235/236)/s6 (Cii, n > 25 muscle fibres) in patient muscle biopsies confirmed the increased
637 phosphorylation of Akt and S6 in the patients (D). Scale bar = 100 μm.

638 (E) Analysis of RNA-seq data from the patient fibroblasts by IPA showed enriched autophagy and
639 unfolded protein response (i) which is associated with activation of PI3K-Akt-mTOR signaling (see Fig.
640 S4A). Immunoblotting of LC3B with chloroquine (CQ, 50 μM for 5 h; n = 4 independent biological

641 samples) or without CQ (n = 7 independent biological samples) in patient fibroblasts (ii, and quantified
642 in iii) suggests an accumulation of LC3BII in the patient cells without an increase in autophagic flux.

643 (F) Confocal imaging of live cells transfected with the autophagy reporter, mCherry-GFP-LC3 in patient
644 fibroblasts (i, n > 100 cells). The ratio of green/red puncta (ii) and autophagosome numbers (iii) were
645 further quantified, showing an increase of these indices. Scale bar = 50 μm in full-scale and 20 μm in
646 zoomed-in images.

647 (G-H) Live cell imaging of mt-Keima expressing control and patient fibroblasts showing mitophagy
648 events at 543 nm excitation. The overlay of mt-Keima emission at 458 nm and ratio image shows the
649 relative level of mitophagy events in control vs patient fibroblasts. (H) The individual mitophagy
650 events, as represented in ratio image, were quantified and plotted as percentage high (F_{543}/F_{458}) ratio
651 area/total mitochondria area, showing a significant reduction in 'mitophagosome' maturation in
652 patient fibroblasts (n≥ 80-100 cells). Scale bar = 20 μm

653 All data, except Figs. 3A and 3Ei, are represented as mean ± S.D. and were analysed by one-way ANOVA
654 with Tukey's multiple comparisons test for fibroblasts and by unpaired t test for biopsies (* $p < 0.05$,
655 ** $p < 0.01$, *** $p < 0.001$, **** $p < 0.0001$).

656

657 **Figure S3. Analysis for RNA-seq of patient fibroblasts with other supporting results and the enriched**
658 **metabolic pathways concordant with the metabolic phenotype of patient fibroblasts.**

659 (A-C) RNA-seq showed by a heatmap (A), a volcano plot (B) and 3D-PCA (C). Gene expression in the
660 mutant cells was significantly distinct from both of the controls: 3394 genes were differentially
661 expressed (FDR < 0.05, with 1849 up-regulated and 1545 down-regulated)

662 (D) Analysis of RNA-seq data from the patient fibroblasts by QIAGEN Ingenuity Pathway Analysis (IPA)
663 showed enriched metabolic pathways ($p < 0.05$) that matchies the findings shown in Figs. 1 and 2.

664 (E) Analysis of the RNA seq data showing a general decrease in mRNA expression of OxPhos-related
665 genes in patient fibroblasts.

666 (F) The mRNA expression of TCA cycle and glycolysis genes in patient fibroblasts confirmed our findings
667 in Fig 2, such as increased pyruvate carboxylase and HK1 expression.

668 (G-H) Analysis of the RNA-seq data showing the mRNA expression associated with amino acid
669 metabolism, including serine/glycine metabolism (G) and amino acid transporters (H).

670 (I) Detailed analysis of the mRNA expression of multiple genes involved in the PI3K-Akt and mTOR
671 pathways in patient fibroblasts, showing consistent differences in a wide array of genes involved in
672 these pathways.

673 (J) Immunoblotting of p-Akt (S473)/Akt, p-S6 (S235/236)/S6 and p-AMPK (T172)/AMPK in A549 cybrid
674 cells (i). (ii) Quantitation shows increased phosphorylation of Akt and S6 but not of AMPK, consistent
675 with the results of fibroblasts (mean ± S.D. of n = 4-5 independent experiments, unpaired t test).

676 (K) Immunoblotting of Akt substrates, p-TSC2 (S939) and p-PRAS40 (T246), and of another mTORC1
677 substrate, p-4EBP1 (S65), in patient fibroblasts grown in the presence of 10% or 1% FBS media shows
678 increased phosphorylation (n = 3 independent experiments, one-way ANOVA with Tukey's multiple
679 comparisons test).

680 All data were analysed as stated above (* $p < 0.05$, *** $p < 0.001$)

681

682 **Figure S4. Other supporting results from patient fibroblasts and A549 cybrid cells for assessing**
683 **autophagy and mitophagy.**

684 (A) H&E and COX staining of patient biopsy.

685 (B) A simple scheme showing the regulation of autophagy and protein translation by the PI3K-Akt-
686 mTORC1 pathway (i). Detailed analysis of the mRNA expression of multiple genes involved in the
687 autophagy in patient fibroblasts, showing consistent differences in a wide array of genes involved (ii).

688 (C-D) Immunoblotting of LC3B ± Bafilomycin A1 (Baf A1, 100 nM) in patient fibroblasts (Ci) and in A549
689 cybrid cells (Di) under basal or starvation conditions (quantified in ii, n = 3-4 independent biological
690 samples) also shows an accumulation of LC3BII in the patient cells without an overall fold increase in
691 autophagic flux that is the conversion of LC3BI to LC3BII.

692 (E) Immunoblotting of LC3B with CQ (50 μM for 5 h; n = 6 independent biological samples) or without
693 CQ (n = 8 independent biological samples) in A549 cybrid cells (i) suggests an accumulation of LC3BII
694 without an increase in autophagic flux (ii) as seen in the patient fibroblasts.

695 (F) Imaging of mCherry-GFP-LC3 (n > 100 cells) in A549 cybrid cells (i). The ratio of green/red puncta
696 (ii) and autophagosome numbers (iii) were further quantified, showing an increase of green/red
697 puncta and total numbers in the mutant cells. Scale bar = 30 μm in full-scale and 10 μm in zoomed-in
698 images.

699 (G) Quantitative analysis of basal autophagy and mitophagy in A549 cybrid cells transfected with
700 COX8-EGFP-mCherry under varied conditions was assessed by flow cytometry using red-to-green
701 fluorescence (n > 3 independent biological samples).

702 All data, except Fig. S4A, are represented as mean ± S.D. and were analysed by one-way ANOVA with
703 Tukey's multiple comparisons test for fibroblasts and by unpaired t test for cybrid cells (* $p<0.05$, **
704 $p<0.01$, *** $p<0.001$, **** $p<0.0001$).

705

706 **Figure 4. Inhibitors of the PI3K-Akt-mTORC1 axis, LY294002 and Rapamycin, reduce mutation load,**
707 **rescue mitochondrial function and reduce glucose dependence.**

708 (A-B) Schematic depicting pharmacological inhibition of the PI3k-Akt-mTORC1 aixs by LY290042 (LY),
709 GDC0941 (GDC), MK2206 (MK) or Rapamycin (RP) (A). (B) Sustained treatment of cells over 6 or 12
710 weeks with LY (5 μM) GDC (1 μM), MK (1 μM) or RP (5 μM) caused a progressive decrease in mutant
711 mtDNA load in A549 cybrid cells (i) and fibroblasts of patient 1 (ii) and suppressed the progressive
712 increase of mutant load with time in culture seen in patient 2 fibroblasts (iii) (n = 3 independent
713 experiments). The concentrations of RP and LY here refer to all subsequent treatments.

714 (C) The mitochondrial membrane potential (TMRM 25 nM) of patient 1 fibroblasts treated with LY,
715 GDC, MK or RP for 12 weeks were significantly increased (n = 13 independent biological samples).
716 Scale bar = 50 μm.

717 (D) The respiratory capacity of patient 1 fibroblasts treated with LY, GDC, MK or RP for 12 weeks was
718 measured using the Seahorse XFe96 extracellular flux analyser and showed a major increase in oxygen
719 consumption under all conditions for the drug-treated cells (n = 14 of culture wells).

720 (E) The $NADH:NAD^+$ ratio of patient 1 fibroblasts treated with LY or RP for 12 weeks was measured
721 using SoNar under basal condition and pyruvate (200 μM, 30 min; i) and quantified (ii; n > 180 cells).
722 The result showed a significant decrease compared to pre-treatment levels. Scale bar = 25 μm.

723 (F) Acidification of the growth medium revealed by the absorption ratio of phenol red was significantly
724 reduced after chronic drug treatments with RP and LY (i and ii; n = 9 culture wells). Lactate production
725 normalised to glucose consumption (iii, n = 4 culture wells) was also significantly reduced. In each
726 case, patient 1 fibroblasts treated with LY or RP for 12 weeks were treated with fresh media and the
727 media were then collected after 48h incubation.

728 (G) Fibroblasts of patient 1 treated with LY or RP for 12 weeks were also cultured in media with a
729 variety of glucose/galactose concentrations to further assess the glucose dependence, displayed a

730 significant improvement of cell growth in all conditions from the drug-treated cells (n = 4-8 culture
731 wells).

732 (H) BNGE were used to assess the expression of respiratory chain proteins and supercomplex assembly
733 of patient 1 fibroblasts treated with LY or RP (i), showing a major increase in the assembly of almost
734 all supercomplexes from the drug-treated cells (ii, n = 3 independent experiments).

735 (I) Rates of ROS production of patient 1 fibroblasts treated with LY or RP for 12 weeks were significantly
736 reduced to the level that lower than or no difference from controls (n = 3-6 independent experiments).

737 All data represented as mean ± S.D. and were analysed by one-way ANOVA with Tukey's multiple
738 comparisons test (* $p < 0.05$, ** $p < 0.01$, *** $p < 0.001$, **** $p < 0.0001$, vs Patient/Mutant control;
739 # $p < 0.05$, ## $p < 0.01$, ### $p < 0.001$, #### $p < 0.0001$, vs WT control).

740

741 **Figure S5. Inhibitors of the PI3K-Akt-mTORC1 axis, LY294002 and Rapamycin, also reduced mutant**
742 **load and rescued mitochondrial function in A549 cybrid cells.**

743 (A) Immunoblotting of the phosphoproteins (p-Akt/Akt, p-mTOR/ mTOR and p-AMPK/AMPK; i) in A549
744 cybrid cells treated with RP (ii) or LY (iii) over 6 weeks demonstrate the effective inhibition of Akt or
745 mTORC1 (n = 3 independent experiments).

746 (B) Immunoblotting of the phosphoproteins (p-Akt/Akt, p-S6/S6 and p-AMPK/AMPK; i) in patient 1
747 fibroblasts treated with RP (ii) or LY (iii) over 12 weeks demonstrated the effective inhibition of Akt or
748 mTORC1 in the drug-treated cells (n = 3-4 independent experiments).

749 (C) Immunoblotting of the phosphoproteins (p-Akt/Akt and p-S6/S6) in A549 cybrid cells (i) and in
750 patient fibroblasts (ii) treated with GDC or MK over 6 weeks demonstrated the effective inhibition of
751 Akt or mTORC1 and upregulated autophagic flux in the drug-treated cells (n = 3 independent
752 experiments).

753 (D) The mitochondrial membrane potential of A549 cybrid cells (i, TMRM 25 nM) significantly
754 increased after exposure to LY, GDC, MK or RP for 6 weeks to the level that only slightly lower than
755 which of WT (ii, n = 8 independent biological samples). Scale bar = 25 μm.

756 (E) Cell respiratory capacity of A549 cybrid cells treated with LY or RP for 6 weeks was measured using
757 the Seahorse XFe96 extracellular flux analyser and showed a major increase in basal and maximum
758 OCR after treatment (n = 18 culture wells).

759 (F) Cytosolic NADH:NAD^+ ratio of A549 cybrid cells transfected with the genetically encoded probe
760 SoNar and treated with LY or RP for 6 weeks was measured (i) and quantified (ii) under basal condition
761 and following exposure to pyruvate (200 μm, 30 min; n > 50 cells).

762 (G) The absorption ratio of phenol red was used to measure the pH of the growth media (i and ii, n=10
763 culture wells) and the kit of the CuBiAn instrument was used to measure lactate production (iii, n = 4
764 culture wells). Both acidification of the medium and lactate secretion (48h incubation) of A549 cybrid
765 cells treated with LY or RP for 6 weeks were reduced.

766 (H) BNGE were used to measure supercomplex assembly and In Gel activity of A549 cybrid cells after
767 6 weeks of treatment with LY or RP (i) and quantified (ii, n = 3 independent experiments).

768 (I) Rates of ROS production of A549 cybrid cells treated with LY or RP for 6 weeks were reduced to the
769 level that no longer significantly different from WT cells (n = 9 culture wells).

770 All data represented as mean ± S.D. and were analysed by one/two-way ANOVA with Tukey's multiple
771 comparisons test (* $p < 0.05$, ** $p < 0.01$, *** $p < 0.001$, **** $p < 0.0001$, vs Patient/Mutant control;
772 # $p < 0.05$, ## $p < 0.01$, ### $p < 0.001$, #### $p < 0.0001$, vs WT control).

773

774 **Figure 5. Reduction of the m.3243A>G mutant load by inhibition of PI3K-Akt-mTORC1 requires**
775 **neither selective cell death nor clonal expansion and is a cell-autonomous event.**

776 (A) A flow chart describing the cell culture process (i) used to assess cell growth/death (ii) over the 4-
777 or 8-week drug pretreatments. Cells were pre-treated with either vehicle, LY, or RP for the time
778 periods as specified in Fig. 5B (pretreatment) and then seeded into 96-well plates for measuring cell
779 growth/death with either vehicle, LY, or RP (treatment). Single cell PCR for the m.3243A>G mutant
780 loads was performed at the end of pretreatments using TaqMan SNP genotyping (iii). (B) Cell growth
781 (i and ii) and cell death (iii and iv) over the 4- or 8-weeks drug treatments of A549 cybrid cells (i and
782 iii) and patient 1 fibroblasts (ii and iv) were measured using Incucyte (n = 6-12 culture wells). Although
783 treatment with either LY or RP at 5 μM slowed cell proliferation in both patient 1 fibroblasts and cybrid
784 cells (i and ii), the cell death numbers were also lowered by the drug treatments (iii and iv).

785 (C-D) A scatter plot showing the distribution of WT and mutant mtDNA measured in single A549 cybrid
786 cells treated with LY or RP for 4 weeks showed a clear shift of mutant load distribution. (C). (D) Mutant
787 load distributions of single A549 cybrid cells (i, n > 850 cells) and patient 1 fibroblasts (ii n > 350 cells)
788 treated with LY or RP for 4 and 8 weeks, respectively.

789 All data represented as mean ± S.D. and were analysed by one/two-way ANOVA with Tukey's multiple
790 comparisons test (* $p < 0.05$, ** $p < 0.01$, *** $p < 0.001$, **** $p < 0.0001$).

791

792 **Figure S6. TaqMan SNP genotyping can be used at single cell resolution to measure the distribution**
793 **of mutant mtDNA burden in a cell population.**

794 (A-B) Cell growth and cell death of A549 cybrid cells were measured before and after treatment with
795 GDC (A, n = 8-16 culture wells) or MK (B, n = 8-20 culture wells) for 4 weeks. The drugs slight inhibited
796 cell growth but had no specific effect on the cell death of mutant cells.

797 (C-D) TaqMan SNP genotyping was validated by measuring the mutation load in a whole population
798 of cells (C, n = 3 independent biological samples) and then to establish the range of mutant load at the
799 level of single cells in the A549 cybrid cells (D).

800 (E) Immunofluorescence staining for MT-COI (i and quantified in ii) showed that the expression of MT-
801 COI in patient 1 fibroblasts was significantly lower than that of control 1 (n > 100 cells), while LY or RP
802 treatments restored its expression (n > 60 of cells). The histograms (iii) display the heterogeneous
803 distribution of intensities measured at the single cell level in control 1 and patient 1 fibroblasts.

804 All data are represented as mean ± S.D. and were analysed by one/two-way ANOVA with Tukey's
805 multiple comparisons test (* $p < 0.05$, ** $p < 0.01$, *** $p < 0.001$, **** $p < 0.0001$).

806

807 **Figure 6. Autophagy/mitophagy is necessary to reduce the m.3243A>G mutant load following**
808 **inhibition of the PI3K-Akt-mTORC1 axis.**

809 (A) In fibroblasts of patient 1, immunoblotting (i) of LC3B with or without CQ (50 μM for 5 h on the
810 day of experiments) over 12 weeks drug treatments (ii and iii) showed a major increase in autophagic
811 flux in drug-treated cells (n = 3-4 of independent experiments).

812 (B) Confocal imaging of the autophagy reporter, mCherry-GFP-LC3 (n > 100 cells) in patient 1
813 fibroblasts treated with LY or RP at the indicated time points (i, 6 weeks, and ii, 24 h). The ratio of
814 green/red puncta (ii) and autophagosome numbers (iii) were further quantified, showing a major
815 decrease in the ratio of green/red puncta in response to the treatments. Scale bar = 50 μm in full-scale
816 and 10 μm in zoomed-in images.

817 (C) Imaging of the mitophagy reporter (i), mt-Keima, was used to specifically quantify mitophagy in
818 patient fibroblasts treated with LY or RP. Quantification of the mitochondrial area fraction engulfed in
819 autolysosomes in both patient 1 (ii) and 2 (iii) were quantified and showed a dramatic increase in

820 mitophagy in both patient cell lines when treated with RP ad LY (n = 82-95 cells), which was completely
821 prevented by treatment with CQ (n = 32-57 cells).

822 (D) A549 cybrid cells (i) and patient 1 fibroblasts (ii) were cultured with the inhibitors RP and LY as in
823 all prior experiments but in combination with CQ (10 μM), showing that CQ completely prevented the
824 decrease of mutant load in response to inhibition of the PI3K-Akt-mTORC1 pathway (n = 3
825 independent experiments).

826 (E) A scheme describing how the m.3243A>G mutation alters cell metabolism, including mitochondrial
827 dysfunction, altered glucose metabolism, redox imbalance and oxidative stress, which leads to the
828 constitutive activation of the PI3K-Akt-mTORC1 pathway and a defect in autophagy/mitophagy.
829 Pharmacological inhibition of this pathway reduces mutant load, rescues mitochondrial function and
830 reduces glucose dependence. These findings suggest that the activation of the PI3K-Akt-mTORC1
831 pathway drives a positive feedback cycle, which maintains/increases mutant mtDNA, augments the
832 metabolic rewiring and thus worsens cell signalling perturbation. This positive feedback loop may
833 shape the phenotype of the disease and determine disease progression.

834 All data are represented as mean ± S.D. and were analysed by one/two-way ANOVA with Tukey's
835 multiple comparisons test (* $p < 0.05$, ** $p < 0.01$, *** $p < 0.001$, **** $p < 0.0001$).

836

837 **Figure S7. Mitochondrial biogenesis and changes in mtDNA copy number do not explain the**
838 **reduction of mutant mtDNA burden, while autophagy/mitophagy is also upregulated by inhibition**
839 **of the PI3K-Akt-mTORC1 pathway in A549 cybrid cells.**

840 (A) Quantitative PCR assessing mtDNA copy numbers of patient 1 fibroblasts (i) and A549 cybrid cells
841 (ii) over the 6- or 12-weeks of treatments (n = 3 independent experiments).

842 (B) In A549 cybrid cells, immunoblotting of LC3B with or without CQ (50 μm for 5 h on the day of
843 experiments) throughout drug treatments (i) showed a major increase in autophagic flux in drug-
844 treated cells (ii and iii, n = 3 independent experiments).

845 (C) Imaging of mCherry-GFP-LC3 (n > 100 cells) in A549 Cybrid cells treated with LY or RP at the
846 indicated time points (i). The ratio of green/red puncta (ii) and autophagosome numbers (iii) were
847 further quantified, showing a major decrease in the ratio of green/red puncta and puncta size. Scale
848 bar = 20 μm in full-scale and 10 μm in zoomed-in images.

849 (D) Analysis of A549 cybrid cells transfected with mCherry-GFP-LC3 under varied conditions (n = 3
850 independent biological samples for each condition) using flow cytometry showed an increase of cells
851 with low GFP intensity when treated with RP and LY, while Baf A1 treatment reversed the effect.

852 (E) Immunoblotting of LC3B (± Baf A1) in A549 cybrid cells (i) and in patient fibroblasts (ii) treated with
853 GDC or MK over 6 weeks demonstrated the upregulated autophagic flux in the drug-treated cells (n =
854 3 independent experiments).

855 (F) Analysis of A549 cybrid cells transfected with COX8-EGFP-mCherry under varied conditions (n = 3
856 independent biological samples for each condition) using flow cytometry showed an increase in
857 proportion of mitophagic positive cells in response to LY, RP and Oligo+AA-induced mitophagy while
858 co-treatment with Baf A1 reversed the effect.

859 (G) Imaging of mt-Keima showing that the increased of mitophagy in patient fibroblasts treated with
860 RP or LY was completely prevented by CQ much higher than patient fibroblasts.

861 (H) Immunoblotting of the phosphoproteins (p-Akt/Akt and p-S6/S6) and LC3B (± Baf A1) in 143B
862 cybrid cells bearing the m.8993T>G mutation showed no difference in protein phosphorylation and
863 autophagic flux among cells with 0% (N0), 50% (N50) and 80% (N80) mutant loads (i, n = 3 independent
864 experiments). PCR-RFLP was applied to measure the change in mutant load in 143B cybrid cells
865 carrying the m.8993T>G mutation treated with LY or RP for 8 weeks, showing no significant effect on
866 the mutant load of the m.8993T>G (ii, n = 3-4 independent biological samples).

867 All data are represented as mean ± S.D. and were analysed by one/two-way ANOVA with Tukey's
868 multiple comparisons test (* $p < 0.05$, ** $p < 0.01$, *** $p < 0.001$, **** $p < 0.0001$).

869 **METHODS**

870 **RESOURCE AVAILABILITY**

871 **Lead Contact**

872 Further information and requests for resources and reagents should be directed to and will be fulfilled
873 by the Lead Contact, Michael R Duchen (m.duchen@ucl.ac.uk).

874

875 **Materials Availability**

876 This study did not generate new unique reagents.

877

878 **Data and Code Availability**

879 Raw and processed RNA-seq data are accessible at the Gene Expression Omnibus under accession
880 GSE175477. Other data including uncropped images of immunoblotting are available in the source
881 and supplementary data.

882

883 **EXPERIMENTAL MODEL AND SUBJECT DETAILS**

884 **Cell Lines**

885 The A549 cybrid cell line derived from the fusion of enucleated patient cells harbouring the
886 m.3243A>G mtDNA mutation was a gift from Ian Holt (Biodondostia Research Institute, San Sebastián,
887 Spain). The 143B cybrid cell lines with ~50% and ~80% of the m.8993T>G mtDNA mutant loads were
888 gifts from the Minczuk lab (MRC Mitochondrial Biology Unit, Cambridge, UK). Control and patient
889 fibroblasts bearing the m.3243A>G mtDNA mutation were obtained from the MRC Centre for
890 Neuromuscular Disorders Biobank London. The patient fibroblasts with the m.3243A>G mutation
891 were isolated from two female subjects (mother and daughter) at the age of 59 (patient 1) and 35
892 (patient 2) at the time biopsies were taken. For patient 1, the clinical symptoms included diabetes,
893 myoclonus, sensorineural hearing loss, memory decline, myopathy, pigmentary retinopathy and
894 bipolar affective disorder. For patient 2, the symptoms included diabetes, sensorineural deafness,
895 cerebellar ataxia, myopathy, epilepsy, depression and cognitive impairment. These cell lines were
896 cultured in Dulbecco's modified Eagle's medium (Gibco #10566016) supplemented with 10% fetal

897 bovine serum (Gibco #16140071), and 1% Antibiotic-Antimycotic (Gibco #15240096) and incubated at
898 37 °C with 5% CO_2.

899

900 **Human muscle biopsies**

901 The muscle biopsies were from a female patient with the m.3243A>G mutation (at the age of 55) and
902 a matched healthy control. The study was approved by the Queen Square Research Ethics Committee,
903 London (09/H0716/76). Informed consent was obtained from all participants.

904

905 **METHOD DETAILS**

906 **Cell culture and drug treatments for PI3K, Akt, or mTORC1 inhibition**

907 A549 cybrid cells (WT and mutant) and 143B cybrid cells were passaged every 3-4 days at 80%
908 confluence and trypsinised using 0.25% trypsin-EDTA (Gibco #25200056). Similarly, control and
909 patient fibroblasts were passaged every week in the same way. Media with or without drugs were
910 changed every 2-3 days. For drug treatments, rapamycin (Cayman Chemical #13346), LY294002
911 (Cayman Chemical #70920) GDC0941 (Cayman Chemical #11600) and MK2206 (Cayman Chemical
912 #11593) were dissolved in DMSO (Sigma-Aldrich #D2650) at 10 mM stock concentrations. For assays
913 to assess autophagy, chloroquine (Cayman Chemical #14194) was dissolved in PBS at 50 mM for stock,
914 while Bafilomycin A1 (Cayman Chemical #11038) was dissolved in DMSO for stock at 200 µM. Drugs
915 were subsequently diluted to their working concentrations in media. Heteroplasmy level in the A549
916 cybrid cells, the 143B cybrid cells and the fibroblasts of patient 1 without treatments did not change
917 significantly throughout the study as assessed by ARMS-qPCR or PCR-RFLP.

918

919 **Measurements for mtDNA mutations**

920 Levels of mtDNA mutation were detected using PCR-restriction fragment length polymorphism
921 (RFLP)[16,48] or allele refractory mutation system (ARMS)-based quantitative PCR (qPCR) analysis[17]. DNA
922 extractions from frozen cells were performed using the DNeasy Blood & Tissue Kit (Qiagen #69506).
923 Concentrations of DNA samples were quantified using NanoDrop. All primer pairs used can be found
924 in Table S5. For PCR-RFLP, samples (20 ng/µl, 2 µl) were mixed with the master mixes containing 1 µl
925 primers (10 µM each) and reagents of GoTaq G2 (Promega #M7845) and the final volume was 25 µl.

926 After 30 thermocycles, amplified PCR products (8 µl) were further digested by ApaI (Promega #R6361)
927 for the m.3243A>G and HapII (Promega #R6311) for the m.8993T>G and analysed by a 2% agarose gel
928 with ethidium bromide. Densitometric analysis was performed by Fiji[49]. For ARMS-qPCR, samples were
929 diluted to 0.4 ng/µl. ARMS primer working solutions (5 µM, 1 µl each) and SYBR Green JumpStart Taq
930 ReadyMix (Sigma-Aldrich #S4438) were added together as master mixes for mutant and wild-type
931 genes. DNA samples (3 µl) and master mixes (7 µl) were pipetted into a 96-well PCR plate (Bio-Rad
932 #MLL9651) and PCR amplification performed using the CFX96 Touch Real-Time PCR Detection System
933 (Bio-Rad). Each sample has three technical replicates. Mutant heteroplasmy level (%) was calculated
934 using $1/[1 + (1/2)^{\Delta CT}] \times 100\%$, where ΔC_T (cycle threshold) = $CT_{wild\text{-}type} - CT_{mutant}$.

935 ARMS-qPCR is a quantitative way to measure mutant loads. In contrast, PCR-RFLP is relatively a
936 qualitative way to detect mtDNA mutations. Due to an intrinsic problem of PCR-RFLP, part of the PCR
937 products are hybrids which have a strand of wild-type (WT) and a strand of mutant, because a single
938 nucleotide mutation is not strong enough to avoid their annealing. Moreover, restriction enzymes
939 cannot recognise and cleavage these hybrids of WT/mutant double strand DNA, which means that in
940 the "WT" band, part of the PCR products are hybrids. Thus, the PCR-RFLP largely underestimates the
941 mtDNA mutant loads, which is the reason why there are weaker hands of the mutant than which of
942 the WT.

943

944 **Quantification of relative mtDNA copy number**

945 The relative mtDNA copy number of cells was determined using quantitative PCR with primers for the
946 mtDNA $tRNA^{Leu(UUR)}$ and with primers for the nuclear B2-microglobulin as previously described[50].
947 Standard 96 well PCR plate with optically clear sealing film and CFX96 Real-Time PCR Detection System
948 (Bio-Rad) were used. PCR mix consists of 2 µl of template DNA (3 ng/µl), 2 µl of primer pair (final
949 concentration of 400 nM), 12.5 µl of SYBR Green JumpStart Taq ReadyMix (Sigma-Aldrich) and 8.5 µl
950 of DNase/RNase free H_2O. The thermal cycling conditions were as follow: 50 °C for 2 min, 95 °C for 10
951 min and then 40 cycles of 95 °C for 15 s and 62 °C for 1 min. Each sample has three technical replicates.
952 The following equation was used to determine the relative mitochondrial DNA content, $2 \times 2^{\Delta CT}$, where
953 ΔC_T is nuclear DNA CT value subtracted by mtDNA CT value.

954

955 **The mitochondrial oxygen consumption rate**

956 Measurements of aerobic respiration and glycolysis were conducted with the Seahorse Bioscience
957 XFe-96 bioanalyzer using the Seahorse XF Cell Mito Stress Test Kit (Agilent #103015-100). Cells were
958 seeded on XF96 cell culture microplates (Agilent #102416-100) two days before the experiment (A549
959 cybrid cells, 1×10^4 cells/well; Fibroblasts, 2×10^4 cells/well). On the day of the experiment, the culture
960 medium was replaced with Seahorse XF Base medium (Agilent #103334-100) supplemented with 1
961 mM pyruvate (Gibco #11360070), 2 mM glutamine (Gibco #25030081) and 10 mM glucose (Gibco
962 #A2494001) and incubated for 30 min at 37 °C in a CO_2-free incubator before loading into the Seahorse
963 Analyzer. After measuring basal respiration, the drugs oligomycin (5 µM), FCCP (1 µM, 2 µM), and
964 rotenone/antimycin A (0.5 µM/0.5 µM) were added to each well in sequential order. Data were
965 analysed using the XF Cell Mito Stress Test Report Generator. After the assay, cells were stained with
966 Hoechst 33342 (5 µM; Thermo Scientific #62249) for 30 min. ImageXpress was then used to count the
967 numbers of cell nuclei (cell numbers) in each well. The normalisation of the experiments is based on
968 the relative cell numbers obtained.

969

970 **Mitochondrial membrane potential ($\Delta\psi_m$)**

971 Cells were seeded (3 x 10^4/well for A549 cybrid cells; 1 x 10^4/well for fibroblasts) in glass-bottom 24-
972 well plates, 2-3 days before imaging. Cells were washed twice with the recording medium, which was
973 phenol red-free DMEM (Gibco #A1443001) with 10 mM glucose, 1 mM glutamine, 10 mM HEPES,
974 adjusted to pH 7.4; and then incubated with 25 nM tetramethylrhodamine methyl ester (TMRM) for
975 30 min at 37 °C. Cells were imaged with an LSM 880 (Carl Zeiss) confocal microscope using Fluar
976 63x/1.40 oil immersion objective lens at 37 °C. TMRM was excited with a 561 nm Argon laser with an
977 output power of 0.2 mW. MBS 488/561 was used as a beam splitter and emitted fluorescence
978 collected at 564-740 nm. Images were acquired using Zen Black software (Carl Zeiss) and fluorescence
979 intensity was quantified using Fiji with the same threshold across all samples.

980

981 **ROS measurements**

982 Rate of general ROS production was assessed using dihydroethidium (DHE, Invitrogen #D11347), an
983 intracellular superoxide indicator which is oxidised by superoxide to ethidium which fluoresces red.
984 As for mitochondrial ROS production, MitoSOX (Invitrogen #M36008) was used. One day before the
985 experiment, cells were seeded in a glass-bottom 96-well plate (SensoPlate #655892) at a density of 2
986 x 10^4 cells per well. On the day of the experiment, cells were washed twice with PBS and incubated

987 with 5 µM DHE or MitoSOX in recording medium (phenol red-free DMEM, 10 mM glucose, 1 mM
988 glutamine, 10 mM HEPES, adjusted to pH 7.4). Measurements of fluorescence intensity were taken at
989 intervals of 5 min at 37 °C using the CLARIOstar microplate reader (excitation/emission = 518/606 nm
990 for DHE excitation/emission = 510/580 nm for MitoSOX). The total incubation time for DHE is 1 h and
991 30 min for MitoSOX. The slope of fluorescence intensity was calculated (Fig. S1C) and represents the
992 rate of ROS production.

993

994 **Glucose uptake using 2-NBDG**

995 A fluorescent deoxyglucose analogue, 2-NBDG (Invitrogen #N13195), was employed as a probe to
996 measure rates of glucose uptake by cultured cells. Cells were seeded in a glass-bottom 96-well plate
997 as ROS measurements. On the day of experiments, cells were firstly washed with glucose-free
998 recording media twice and incubated with the glucose-free media for 1 h. After media aspiration,
999 recording media with 2-NBDG (100 µg/ml) were then added into wells and incubated for 30 min. After
1000 the incubation, cells were then again washed with glucose-free recording media twice and
1001 fluorescence intensity were measured using the CLARIOstar microplate reader (excitation/emission =
1002 467/542 nm).

1003

1004 **Medium pH values**

1005 Medium pH values were measured based on the ratiometric property of phenol red, a common pH
1006 indicator in media. The absorbance of phenol red change in response to changing pH. Cells were
1007 seeded in 96-well plates at a density of 1 x 10^4 cells per well with 200 µl media and cultured for 2 days.
1008 On the day of experiments, media of each well were then transferred to a new 96-well plate and
1009 measured the absorbance of phenol red at 443 and 570 nm immediately. The higher the absorbance
1010 ratios of 443 to 570 nm, the more acidic the media.

1011

1012 **Glucose and lactate concentrations in media using CuBiAn**

1013 Media for pH measurements were then directly used for quantifying glucose and lactate
1014 concentrations in media. Samples and fresh media were measured using the CuBiAn HT-270
1015 biochemistry analyser (Optocell technology) with its Glucose (#200106) and Lactate Assay Kits
1016 (#200115) according to manufacturer instructions.

1017

1018 **Blue native gel electrophoresis (BNGE) and In Gel activity assays**

1019 Mitochondria were isolated from cultured fibroblasts and cell lines according to the method described
1020 earlier (ref). Digitonin-solubilized mitochondria proteins (100 µg) were separated on pre-cast 3%-12%
1021 gradient blue native gels (Invitrogen #BN1001) according to manufacturer's instructions. After
1022 electrophoresis, the gels were electroblotted onto PVDF membrane (Millipore #IPVH00010) and
1023 probed with anti-OxPhos antibody cocktail (1:1000, Invitrogen #45-8199), anti-SDHA (1:1000, Abcam
1024 #ab137040) and anti-ATP5A (1:1000, Abcam #ab14748). The enzymatic activity of different OxPhos
1025 complexes was determined by in-gel assays. For CIV+CI activity, the gels were incubated first in CIV
1026 substrate (50 mg diaminobenzidine and 100 mg cytochrome c in 50 mM phosphate buffer, pH 7.4)
1027 until brown signal was observed and then incubated in CI substrate (0.1 mg/ml NADH, 2.5 mg/ml
1028 Nitrotetrazolium Blue chloride in 100 mM Tris–HCl, pH 7.4) until blue signal appeared. The reaction
1029 was stopped with 10% acetic acid and the gels were washed and scanned.

1030

1031 **SDS-PAGE and immunoblotting**

1032 For immunoblotting, cells were seeded 1-day prior experiments (60 mm plates for the A549 cybrid
1033 cells and 10 cm plates for fibroblasts). To assess autophagic flux, cells were replenished with regular
1034 media for 1 h to prevent starvation-induced autophagy. After 1 h, treatment conditions resumed
1035 either with or without 50 µM chloroquine for 6 h. For other experiments, cells were then washed with
1036 ice-cold PBS once and lysed using 150-300 µl RIPA buffer (Sigma-Aldrich #R0278) with one cOmplete™
1037 Protease Inhibitor Cocktail (Roche #4693116001) tablet and one PhosSTOP Phosphatase Inhibitor
1038 Cocktail (Roche #4906837001) tablet. Cells were then scraped and centrifuged at 16,000 g at 4 °C for
1039 30 min. Protein concentration in the supernatant was quantified using the Pierce BCA Assay Kit
1040 (Thermo Scientific #23227). For immunoblotting, 30 µg of protein samples in NuPAGE 4x LDS Sample
1041 Buffer (Invitrogen #NP0007) and 2% β-mercaptoethanol (Sigma-Aldrich #63689) were boiled at 99ºC
1042 for 5 min. Proteins were separated on 4-12% NuPAGE Bis-Tris polyacrylamide gels (Invitrogen
1043 #NP0335) or 12% Bis-Tris gels (#NW00122) immersed in MOPS running buffer (Invitrogen #NP0001)
1044 and transferred onto PVDF membranes (Millipore #IPFL00010). Membranes were then incubated in
1045 Intercept (TBS) Blocking Buffer (Li-COR Biosciences #927-60001) for 1 h at room temperature. After
1046 addition of primary antibodies diluted in the blocking buffer with 0.1% Tween-20, membranes were
1047 incubated overnight at 4ºC on a shaker. Subsequently, membranes were incubated with appropriate
1048 secondary antibodies (Li-COR Biosciences; 1:10000; IRDye® 680RD Goat anti-Mouse IgG, #926-68070;

1049 IRDye® 800CW Goat anti-Rabbit IgG, #926-32211) for 1 h at room temperature before signals were
1050 developed with the LiCOR Odyssey CLx system. Details of all the antibodies used in this study can be
1051 found in the Key Resources Table. Following is the antibodies and dilutions for immunoblotting: Anti-
1052 PC (1:1000, Novus Biologicals #NBP1-49536), anti-phospho-PDHA (1:1000, Millipore #AP1062), anti-
1053 PDHA (1:1000, Invitrogen #45-6600), anti-p-Akt (1:1000, Cell Signaling Technology #9271), anti-Akt
1054 (1:3000, Cell Signaling Technology #9272), anti-p-S6 (1:3000, Cell Signaling Technology #4858), anti-
1055 S6 (1:3000, Cell Signaling Technology #2217), anti-p-AMPK (1:1000, Cell Signaling Technology #2532),
1056 anti-AMPK (1:3000, Cell Signaling Technology #2532), anti-LC3B (1:3000, Cell Signaling Technology
1057 #3868), and anti-β-actin (1:10000, Santa Cruz Biotechnology #sc-47778).

1058

1059 **Live-cell imaging for cell growth and death using the Incucyte platform**

1060 Cells were seeded at a density of 2,000 cells/well in a 96-well plate one-day prior imaging with regular
1061 cell culture media. For cell growth/death in a variety of nutrient conditions, cells were washed with
1062 PBS twice and then DMEM (Gibco #11966025 or #11960044) with different concentration of glucose,
1063 galactose (Sigma-Aldrich #G5388) or glutamine and 10% dialysed FBS (Sigma-Aldrich #F0392) were
1064 added. For drug treatments, media were then replaced with fresh media with/without drugs along
1065 with 20 nM SYTOGreen Nucleic Acid Stain (Invitrogen #S7572) just before imaging. Images were
1066 acquired using the Incucyte with 20X objective every 2 h for a 3-4 day period. Cell confluency and cell
1067 death numbers were analysis on Incucyte software and sequentially extracted. Rates of cell growth
1068 were analysed by fitting the growth curve to the exponential cell growth model (Fig. S1E) using the
1069 solver in Excel, while cell death was obtained by simply normalising the numbers of dead cells
1070 (SYTOGreen stained) to total cell confluency.

1071

1072 **Measurements of cytosolic NADH:NAD$^+$ using SoNar**

1073 The genetically encoded probes, SoNar for NADH:NAD$^+$ ratio, were developed by and obtained from
1074 the Yang's Lab (Chinese Academy of Sciences)[18]. For A549 cybrid cells, the cells were seeded at the
1075 density of 4 x 10^4/well in glass-bottom 24-well plates two days before transfection. Lipofectamine
1076 3000 (Invitrogen #L3000001) was used for transfection according to the manufacturer's protocol.
1077 Specifically, we used 1 µg DNA and the ratio of p3000 to the 3000 reagent was 2:1. The cells were
1078 imaged two days after transfection in recording media with the LSM 880 microscope using 20x/0.8
1079 objective lens at 37ºC. Both probes were excited at 405 and 488 separately and emitted fluorescence

1080 longer than 535 nm was collected. For fibroblasts, Human Dermal Fibroblasts Nucleofector Kit (Lonza
1081 #VPD-1001) was used for transfection according to the manufacturer's protocol. Specifically, we used
1082 2.5 µg DNA for 5 x 10^5 cells. Similarly, fibroblasts were imaged two days after transfection with the
1083 same conditions as A549 cybrid cells. Images were acquired using Zen Black software (Carl Zeiss) and
1084 analysed using Fiji. Regions of interest (ROI) were generated by thresholding and binarizing images
1085 and average fluorescence intensity in the ROIs for each channel were then measured. Ratios between
1086 the signal excited at 405 nm and 488 nm were calculated.

1087

1088 **Measurement of autophagy and mitophagy using mCherry-EGFP-LC3 and mt-Keima/COX8-EGFP-**
1089 **mCherry reporters, respectively**

1090 The autophagy reporter, mCherry-EGFP-LC3 (Addgene plasmid #22418), and mitophagy reporter, mt-
1091 Keima (Addgene plasmid #56018) and COX8-EGFP-mCherry (Addgene plasmid #78520), were
1092 purchased from Addgene. The procedure of transfection for A549 cybrid cells and patient fibroblasts
1093 was similar to SoNar. Imaging was performed with the LSM 880 microscope using 63x/1.40 oil
1094 immersion objective lens at 37 °C. The mCherry-EGFP-LC3 was excited at 488 and 561 nm separately
1095 and emitted fluorescence 500-580 and longer than 600 nm was collected. Images were acquired using
1096 Zen Black software (Carl Zeiss). Numbers and area of fluorescent particles for each channel were
1097 quantified using Fiji by thresholding images. For mt-Keima, following transfection, the cells were
1098 treated as indicated for 24h and imaged via two sequential excitations (458 nm, green; 561 nm, red)
1099 using a 570- to 695-nm emission range. The laser power was set at the minimum output to allow the
1100 clear visualization of the mt-Keima signal and was separately adjusted for each experimental
1101 condition. At least 10 z-stacks with 0.45 um thickness were acquired per sample in an experimental
1102 set. LysoTracker Green DND-26 (Invitrogen #L7526) was co-imaged using a 488 nm excitation and a
1103 495-550 nm emission filter, where indicated. The ratio (high F_{543}/F_{458} ratio area/total mitochondrial
1104 area) was used as an index of mitophagy. Ratio (F_{543}/F_{458}) images were generated using the Ratio Plus
1105 plugin in Fiji. High (F_{543}/F_{458}) ratio areas and total mitochondrial area were binarized, segmented and
1106 quantified in Fiji. Quantitative analysis of mitophagy in COX8-EGFP-mCherry-transfected A549 cybrid
1107 cells was also assessed using a flow cytometry-based approach in which an arbitrary threshold of red
1108 fluorescence signal was used to indicate a mitophagic positive cell. Following transfection, cells were
1109 treated with either DMSO or different drugs as indicated. After 24 h. of treatment, cells were
1110 trypsinized, washed once with DPBS and then resuspended into 1 ml of DPBS prior to analysis using a
1111 BD Accuri C6 flow cytometer. Cells were excited with a 488 nm laser with emission assessed

1112 simultaneously using a 533/30 nm (FL1 detector) and a 670 LP filter (FL3 detector). Cells with high
1113 FL3/FL1 ratio were selected and their proportion was calculated.

1114

1115 **Metabolomics**

1116 Control and patient fibroblasts were plated 24 hrs before the experiment in 10 cm dishes (1 x 10^6
1117 cells/dish). On the day of experiments, the medium was replaced with phenol red-free DMEM with 1
1118 mM glutamine, 10% dialysed FBS (prepared as described in Yuneva et al., 2007) and 10 mM [U-^{13}C]-
1119 glucose (Goss Scientific #CLM-1396-1). After 24 h incubation, cells were washed once with ice-cold
1120 PBS. Metabolites were extracted with adding 500 µl of ice-cold methanol, scraping, and transferring
1121 into tubes on ice. Dishes were then subsequently washed with 250 µl methanol and 250 µl water
1122 containing 2.5 nM of each nor-leucine and scyllo-inositol per sample as internal standards. Finally, 250
1123 µl of chloroform was added and samples were sonicated for 3 rounds (8 min each) at 4 °C. After
1124 centrifugation (18,000 g for 10 min at 4 °C), the upper polar fraction was collected and used for GC-
1125 MS analysis, while he protein pellets were dried, lysed using 62.5 mM Tris buffer (pH 6.8) containing
1126 2% SDS and used for protein quantification using BCA assay (Abcam). Briefly, the polar fraction was
1127 washed twice with methanol, derivatized by methoximation (Sigma, 20 µl, 20 mg/ml in pyridine) and
1128 trimethylsilylation (20 µl of N,O-bis(trimethylsilyl) trifluoroacetamide reagent (BSTFA) containing 1%
1129 trimethylchlorosilane (TMCS), Supelco), and analysed on an Agilent 7890A-5975C GC–MS system.
1130 Splitless injection (injection temperature 270 °C) onto a 30 m + 10 m × 0.25 mm DB-5MS + DG column
1131 (Agilent J&W) was used, using helium as the carrier gas, in electron ionization (EI) mode. The initial
1132 oven temperature was 70 °C (2 min), followed by temperature gradients to 295 °C at 12.5 °C/min and
1133 then to 320 °C at 25 °C/min (held for 3 min). Data analysis and peak quantifications were performed
1134 using MassHunter Quantitative Analysis software (B.06.00 SP01, Agilent Technologies). The level of
1135 labelling of individual metabolites was corrected for the natural abundance of isotopes in both the
1136 metabolite and the derivatization reagent. Abundance was calculated by comparison to responses of
1137 known amounts of authentic standards[52]. The data were further processed and visualised by
1138 MetaboAnalyst 5.0, using the Pathway Analysis module (data were normalised to controls and scaled
1139 by the standard deviation of each variable) with the library of human SMPDB[53].

1140

1141 **RNA-sequencing**

1142 Fibroblasts for RNA-sequencing were plated in 10 cm dishes with regular media (1 x 10^6 cells/dish) one
1143 day before RNA extraction. RNA extractions were performed using the RNeasy Mini Kit (Qiagen
1144 #74104). Concentrations and quality of RNA samples were quantified using NanoDrop (total RNA >250
1145 ng, A_{260}/A_{280} = 1.8-2.1, A_{260}/A_{230} > 1.7). RNA-sequencing was then performed at UCL Genomics and
1146 analysed by the SARTools R package[54]. The resulting datasets were further analysed by Ingenuity
1147 Pathway Analysis (IPA, Qiagen) with a threshold of FDR < 0.05 and visualised by Morpheus
1148 (https://software.broadinstitute.org/morpheus) for heatmaps and NetworkAnalyst 3.0[55] for volcano
1149 plots and principal component analysis.

1150

1151 **Immunohistochemistry**

1152 For immunohistochemistry, muscle biopsies were fixed in phosphate buffered saline (PBS) and fixed
1153 in 4% paraformaldehyde (PFA), made in PBS, for 4-8 h at room temperature (RT). Following fixation,
1154 tissues were cryoprotected in 30% sucrose in Diethyl Pyrocarbonate (DEPC) treated PBS, embedded
1155 and frozen in a mixture of 15% sucrose /50% Tissue-Tek OCT (Sakura Finetek), and sectioned in the
1156 coronal plane at 20 µm using a Cryostat (Bright Instruments). Patient muscle biopsies sections were
1157 washed in PBS, blocked in a solution of 5% normal goat serum (Merck KGaA) (v/v) containing 0.1%
1158 Triton X-100 (v/v) (Merck KGaA) in PBS at RT for 2 h. They were first incubated in primary antibodies
1159 at RT overnight. The following antibodies were used: pan-AKT (1:200, Cell Signaling Technology
1160 #2920), phospho-AKT (p-AKT; 1:200, Abcam #ab81283), S6 (1:200), and phospho-S6 (1:200). Following
1161 incubation in primary antibodies, sections were washed in PBS, incubated in biotinylated anti-species
1162 secondary antibodies (1:250; Vector Laboratories) for 2 h. Sections were washed and incubated with
1163 bisbenzimide (10 min in 2.5 µg/ml solution in PBS; Merck KGaA). Images were collected using an SP2
1164 Leica confocal microscope (Leica Microsystems, UK). Sequential images were subsequently
1165 reconstructed using Metamorph imaging software (Universal Imaging Corporation, West Chester, PA).

1166

1167 **Immunofluorescence**

1168 Fibroblasts were seeded at a density of 5 x 10^4 cells/well in 24 well plates on 10 mm coverslips. After
1169 24h incubation, cells were treated with LY or RP for 4 weeks and 8 weeks respectively. After the long-
1170 term treatment, the cells were washed thrice with 1X PBS and fixed in 4% paraformaldehyde for 15
1171 mins at room temperature and permeabilised with 0.1% Triton-X 100 for 15 min in PBS. The cells were
1172 then washed and incubated with anti-MTCOI antibody (1:100, Abcam #ab14705) in 3% BSA for 1h at
1173 the room temperature followed by incubation with Alexa Fluor 488-conjugated secondary antibody

1174 for 1h at the room temperature. After antibody labelling, the coverslips were mounted on a glass slide
1175 using ProLong™ Gold Antifade mountant with DAPI and imaged using the confocal microscope as
1176 described above.

1177

1178 **TaqMan SNP genotyping for Single cell qPCR**

1179 Primers for distinguishing WT and the m.3243A>G mutant mtDNA were designed by submitting the
1180 region of the m.3243A>G mutation (~120 bp) to the website of online Custom TaqMan® Assay design
1181 tool (https://www.thermofisher.com/order/custom-genomic-products/tools/genotyping/) The
1182 Custom TaqMan SNP Genotyping Kit (Applied Biosystems #4332073) was ordered and prepared
1183 according to manufacturer instructions. For single cell sorting, cells were resuspended (1 x 10^6 cells/ml
1184 for A549 cybrid cells; 5 x 10^5 cells/ml for fibroblasts) in 1 ml PBS with 1% FBS, filtered through 70 µm
1185 mesh and then kept on ice. Sorting cells to 96-well PCR plates using BD FACS Aria Fusion was
1186 performed by Flow Cytometry Core Facility, Division of Medicine at UCL. Cells in 96-well plates were
1187 lysed with 2 µl of 0.2% Triton X-100 and kept in -80 °C immediately. For qPCR, TaqPath ProAmp Master
1188 Mix (Applied Biosystems #A30866) was mixed with primers of TaqMan SNP genotyping and added into
1189 96-well PCR plates to reach a final volume of 10 µl in each well. Thermo cycles were set according to
1190 manufacturer instructions. Mutant loads were determined by the ratio of mutant to total fluorescent
1191 intensity.

1192

1193 **Quantification and statistical analysis**

1194 All statistical analyses, unless otherwise stated in figure legends, were carried out using GraphPad
1195 Prism 8. To compare means between two groups, a two-tailed unpaired t-test was used for normally
1196 distributed data. One/two-way ANOVA with Tukey's multiple comparisons test was performed for
1197 multi-group (at least three) comparisons. Data are presented as graphs displaying mean ± S.D., of at
1198 least three independent biological replicates. Means of control samples on immunoblotting or
1199 immunofluorescence are typically centred at one (or 100%) to ensure easier comparisons unless
1200 otherwise noted. Differences were only considered to be statistically significant when the *p* value was
1201 less than 0.05. Estimated *p* values are either stated as the actual values or denoted by * $p < 0.05$, ** p
1202 < 0.01, *** $p < 0.001$, **** $p < 0.0001$.

1203 For detailed processing and statistical analysis of RNA sequencing and metabolomics, please find them
1204 in the previous section with the same subheadings.

1205 No statistical method was used to predetermine sample size, and replicates are shown in Figure
1206 legends. The investigators were not blinded to allocation during experiments and outcome
1207 assessment.

1208 **REFERENCES**

1209 1. Gorman, G. S. *et al.* Prevalence of nuclear and mitochondrial DNA mutations related to adult
1210 mitochondrial disease. *Ann. Neurol.* (2015) doi:10.1002/ana.24362.

1211 2. Russell, O. M., Gorman, G. S., Lightowlers, R. N. & Turnbull, D. M. Mitochondrial Diseases: Hope
1212 for the Future. *Cell* **181**, 168–188 (2020).

1213 3. Craven, L., Alston, C. L., Taylor, R. W. & Turnbull, D. M. Recent Advances in Mitochondrial
1214 Disease. *Annu Rev Genomics Hum Genet* **18**, 257–275 (2017).

1215 4. Schon, E. A., DiMauro, S. & Hirano, M. Human mitochondrial DNA: roles of inherited and
1216 somatic mutations. *Nat Rev Genet* **13**, 878–890 (2012).

1217 5. Szczepanowska, J., Malinska, D., Wieckowski, M. R. & Duszynski, J. Effect of mtDNA point
1218 mutations on cellular bioenergetics. *Biochim. Biophys. Acta - Bioenerg.* **1817**, 1740–1746
1219 (2012).

1220 6. Stewart, J. B. & Chinnery, P. F. The dynamics of mitochondrial DNA heteroplasmy: implications
1221 for human health and disease. *Nat. Rev. Genet.* **16**, 530 (2015).

1222 7. Maeda, K. *et al.* Clinical Phenotype and Segregation of Mitochondrial 3243A>G Mutation in
1223 2 Pairs of Monozygotic Twins. *JAMA Neurol.* **73**, 990–993 (2016).

1224 8. Picard, M. & Hirano, M. Disentangling (Epi)Genetic and Environmental Contributions to the
1225 Mitochondrial 3243A>G Mutation Phenotype: Phenotypic Destiny in Mitochondrial
1226 Disease? *JAMA Neurol.* **73**, 923–925 (2016).

1227 9. Kotiadis, V. N., Duchen, M. R. & Osellame, L. D. Mitochondrial quality control and
1228 communications with the nucleus are important in maintaining mitochondrial function and cell
1229 health()(). *Biochim. Biophys. Acta* **1840**, 1254–1265 (2014).

1230 10. Valera-Alberni, M. & Canto, C. Mitochondrial stress management: a dynamic journey. *Cell*
1231 *Stress* **2**, 253–274 (2018).

1232 11. Gilkerson, R. W. *et al.* Mitochondrial autophagy in cells with mtDNA mutations results from
1233 synergistic loss of transmembrane potential and mTORC1 inhibition. *Hum Mol Genet* **21**, 978–
1234 990 (2012).

1235 12. Morán, M. *et al.* Bulk autophagy, but not mitophagy, is increased in cellular model of

1236 mitochondrial disease. *Biochim. Biophys. Acta - Mol. Basis Dis.* **1842**, 1059–1070 (2014).

1237 13. Deus, C. M., Yambire, K. F., Oliveira, P. J. & Raimundo, N. Mitochondria–Lysosome Crosstalk:
1238 From Physiology to Neurodegeneration. *Trends Mol. Med.* **26**, 71–88 (2020).

1239 14. Plotegher, N. & Duchen, M. R. Mitochondrial Dysfunction and Neurodegeneration in Lysosomal
1240 Storage Disorders. *Trends Mol. Med.* **23**, 116–134 (2017).

1241 15. Cotán, D. *et al.* Secondary coenzyme Q10 deficiency triggers mitochondria degradation by
1242 mitophagy in MELAS fibroblasts. *FASEB J.* **25**, 2669–2687 (2011).

1243 16. Nigou, M., Parfait, B., Clauser, E. & Olivier, J. L. Detection and quantification of the A3243G
1244 mutation of mitochondrial DNA by ligation detection reaction. *Mol. Cell. Probes* **12**, 273–282
1245 (1998).

1246 17. Wang, J., Venegas, V., Li, F. & Wong, L. J. Analysis of mitochondrial DNA point mutation
1247 heteroplasmy by ARMS quantitative PCR. *Curr Protoc Hum Genet* **Chapter 19**, Unit 19 6 (2011).

1248 18. Zhao, Y. *et al.* SoNar, a Highly Responsive NAD+/NADH Sensor, Allows High-Throughput
1249 Metabolic Screening of Anti-tumor Agents. *Cell Metab* **21**, 777–789 (2015).

1250 19. El-Hattab, A. W., Adesina, A. M., Jones, J. & Scaglia, F. MELAS syndrome: Clinical manifestations,
1251 pathogenesis, and treatment options. *Mol. Genet. Metab.* **116**, 4–12 (2015).

1252 20. Manning, B. D. & Toker, A. AKT/PKB Signaling: Navigating the Network. *Cell* **169**, 381–405
1253 (2017).

1254 21. N'Diaye, E.-N. *et al.* PLIC proteins or ubiquilins regulate autophagy-dependent cell survival
1255 during nutrient starvation. *EMBO Rep.* **10**, 173–179 (2009).

1256 22. Deng, J. *et al.* RNA-seq profiling, and impaired autophagic process in skeletal muscle of MELAS.
1257 *Biochem. Biophys. Res. Commun.* **523**, 91–97 (2020).

1258 23. Garrido-Maraver, J. *et al.* Critical role of AMP-activated protein kinase in the balance between
1259 mitophagy and mitochondrial biogenesis in MELAS disease. *Biochim Biophys Acta* **1852**, 2535–
1260 2553 (2015).

1261 24. Janssen, G. M. C. *et al.* The A3243G tRNALeu(UUR) mutation induces mitochondrial dysfunction
1262 and variable disease expression without dominant negative acting translational defects in
1263 complex IV subunits at UUR codons†. *Hum. Mol. Genet.* **16**, 2472–2481 (2007).

1264 25. Suen, D.-F., Narendra, D. P., Tanaka, A., Manfredi, G. & Youle, R. J. Parkin overexpression
1265 selects against a deleterious mtDNA mutation in heteroplasmic cybrid cells. *Proc. Natl. Acad.*
1266 *Sci.* **107**, 11835 LP – 11840 (2010).

1267 26. Kandul, N. P., Zhang, T., Hay, B. A. & Guo, M. Selective removal of deletion-bearing
1268 mitochondrial DNA in heteroplasmic Drosophila. *Nat. Commun.* **7**, 13100 (2016).

1269 27. Gaude, E. *et al.* NADH Shuttling Couples Cytosolic Reductive Carboxylation of Glutamine with
1270 Glycolysis in Cells with Mitochondrial Dysfunction. *Mol. Cell* **69**, 581-593.e7 (2018).

1271 28. Wojewoda, M., Duszyński, J. & Szczepanowska, J. NARP mutation and mtDNA depletion trigger
1272 mitochondrial biogenesis which can be modulated by selenite supplementation. *Int. J.*
1273 *Biochem. Cell Biol.* **43**, 1178–1186 (2011).

1274 29. de Andrade, P. B. M. *et al.* Diabetes-associated mitochondrial DNA mutation A3243G impairs
1275 cellular metabolic pathways necessary for beta cell function. *Diabetologia* **49**, 1816–1826
1276 (2006).

1277 30. Chen, Q. *et al.* Rewiring of Glutamine Metabolism Is a Bioenergetic Adaptation of Human Cells
1278 with Mitochondrial DNA Mutations. *Cell Metab.* **27**, 1007-1025.e5 (2018).

1279 31. Cappel, D. A. *et al.* Pyruvate-Carboxylase-Mediated Anaplerosis Promotes Antioxidant Capacity
1280 by Sustaining TCA Cycle and Redox Metabolism in Liver. *Cell Metab.* **29**, 1291-1305.e8 (2019).

1281 32. Mick, E. *et al.* Distinct mitochondrial defects trigger the integrated stress response depending
1282 on the metabolic state of the cell. *Elife* **9**, (2020).

1283 33. Raimundo, N. *et al.* Mitochondrial Stress Engages E2F1 Apoptotic Signaling to Cause Deafness.
1284 *Cell* **148**, 716–726 (2012).

1285 34. Hoxhaj, G. & Manning, B. D. The PI3K–AKT network at the interface of oncogenic signalling and
1286 cancer metabolism. *Nat. Rev. Cancer* **20**, 74–88 (2020).

1287 35. Koromilas, A. E. & Mounir, Z. Control of oncogenesis by eIF2α phosphorylation: implications in
1288 PTEN and PI3K–Akt signaling and tumor treatment. *Futur. Oncol.* **9**, 1005–1015 (2013).

1289 36. Suomalainen, A. & Battersby, B. J. Mitochondrial diseases: the contribution of organelle stress
1290 responses to pathology. *Nat Rev Mol Cell Biol* **19**, 77–92 (2018).

1291 37. Quirós, P. M. *et al.* Multi-omics analysis identifies ATF4 as a key regulator of the mitochondrial

1292 stress response in mammals. *J. Cell Biol.* **216**, 2027–2045 (2017).

1293 38. Khan, N. A. *et al.* mTORC1 Regulates Mitochondrial Integrated Stress Response and
1294 Mitochondrial Myopathy Progression. *Cell Metab* **26**, 419-428 e5 (2017).

1295 39. Lin, Y.-F. *et al.* Maintenance and propagation of a deleterious mitochondrial genome by the
1296 mitochondrial unfolded protein response. *Nature* **533**, 416 (2016).

1297 40. Picard, M. *et al.* Progressive increase in mtDNA 3243A>G heteroplasmy causes abrupt
1298 transcriptional reprogramming. *Proc Natl Acad Sci U S A* **111**, E4033-42 (2014).

1299 41. McMillan, R. P. *et al.* Quantitative Variation in m.3243A > G Mutation Produce Discrete
1300 Changes in Energy Metabolism. *Sci. Rep.* **9**, 5752 (2019).

1301 42. Chae, S. *et al.* A Systems Approach for Decoding Mitochondrial Retrograde Signaling Pathways.
1302 *Sci. Signal.* **6**, rs4 LP-rs4 (2013).

1303 43. Civiletto, G. *et al.* Rapamycin rescues mitochondrial myopathy via coordinated activation of
1304 autophagy and lysosomal biogenesis. *EMBO Mol Med* **10**, (2018).

1305 44. Zheng, X. *et al.* Alleviation of neuronal energy deficiency by mTOR inhibition as a treatment for
1306 mitochondria-related neurodegeneration. *Elife* **5**, (2016).

1307 45. Haroon, S. *et al.* Multiple Molecular Mechanisms Rescue mtDNA Disease in C. elegans. *Cell Rep*
1308 **22**, 3115–3125 (2018).

1309 46. Johnson, S. C. *et al.* mTOR Inhibition Alleviates Mitochondrial Disease in a Mouse Model of
1310 Leigh Syndrome. *Science (80-.).* **342**, 1524 LP – 1528 (2013).

1311 47. Barriocanal-Casado, E. *et al.* Rapamycin administration is not a valid therapeutic strategy for
1312 every case of mitochondrial disease. *EBioMedicine* **42**, 511–523 (2019).

1313 48. White, H. E. *et al.* Accurate Detection and Quantitation of Heteroplasmic Mitochondrial Point
1314 Mutations by Pyrosequencing. *Genet. Test.* **9**, 190–199 (2005).

1315 49. Schindelin, J. *et al.* Fiji: an open-source platform for biological-image analysis. *Nat. Methods* **9**,
1316 676–682 (2012).

1317 50. Rooney, J. P. *et al.* PCR based determination of mitochondrial DNA copy number in multiple
1318 species. *Methods Mol Biol* **1241**, 23–38 (2015).

1319 51. Yuneva, M., Zamboni, N., Oefner, P., Sachidanandam, R. & Lazebnik, Y. Deficiency in glutamine
1320 but not glucose induces MYC-dependent apoptosis in human cells . *J. Cell Biol.* **178**, 93–105
1321 (2007).

1322 52. Méndez-Lucas, A. *et al.* Identifying strategies to target the metabolic flexibility of tumours. *Nat.*
1323 *Metab.* **2**, 335–350 (2020).

1324 53. Chong, J., Wishart, D. S. & Xia, J. Using MetaboAnalyst 4.0 for Comprehensive and Integrative
1325 Metabolomics Data Analysis. *Curr. Protoc. Bioinforma.* **68**, e86 (2019).

1326 54. Varet, H., Brillet-Guéguen, L., Coppée, J.-Y. & Dillies, M.-A. SARTools: A DESeq2- and EdgeR-
1327 Based R Pipeline for Comprehensive Differential Analysis of RNA-Seq Data. *PLoS One* **11**,
1328 e0157022 (2016).

1329 55. Xia, J., Gill, E. E. & Hancock, R. E. W. NetworkAnalyst for statistical, visual and network-based
1330 meta-analysis of gene expression data. *Nat. Protoc.* **10**, 823–844 (2015).

1331

1332 **ACKNOWLEDGEMENTS**

1333 We thank Alice Giustacchini (UCL ICH) for help with single cell analyses, Stephanie Carrington (Division
1334 of Neuropathology, UCL IoN) for sectioning the muscle biopsies, Ash Merve (Consultant
1335 Neuropathologist, Division of Neuropathology, UCL IoN and Department of Histopathology, Camelia
1336 Botnar Laboratory, Great Ormond Street Hospital) for reviewing the biopsy and taking H&E staining
1337 images, and Metabolomics STP of the Francis Crick Institute for assistance with GC-MS analysis. We
1338 also acknowledge The MRC Centre for Neuromuscular Diseases Biobank (supported by the National
1339 Institute for Health Research Biomedical Research Centres at Great Ormond Street Hospital for
1340 Children NHS Foundation Trust and at University College London Hospitals NHS Foundation Trust and
1341 University College London) for providing all patient-derived cells used in this study. RDSP is supported
1342 by a Medical Research Council (UK) Clinician Scientist Fellowship (MR/S002065/1) and a Medical
1343 Research Council (UK) strategic award to establish an International Centre for Genomic Medicine in
1344 Neuromuscular Diseases (ICGNMD) (MR/S005021/1). GS is supported by Telethon GGP16026 and
1345 CRUK Pioneer Award C28472/A29264. MY is supported by the Francis Crick Institute which receives
1346 its core funding from Cancer Research UK (FC001223), the UK Medical Research Council (FC001223),
1347 and the Wellcome Trust (FC001223). GEV is supported by the National Agency for Research and
1348 Development (ANID) / Scholarship Program / DOCTORADO BECAS CHILE/2019 – 7220052 We also
1349 thank Action Medical Research for funding the early stages of this work and the Ministry of Education,

Taiwan for funding CYC's PhD by the Government Scholarship to Study Abroad.

Fig. 1

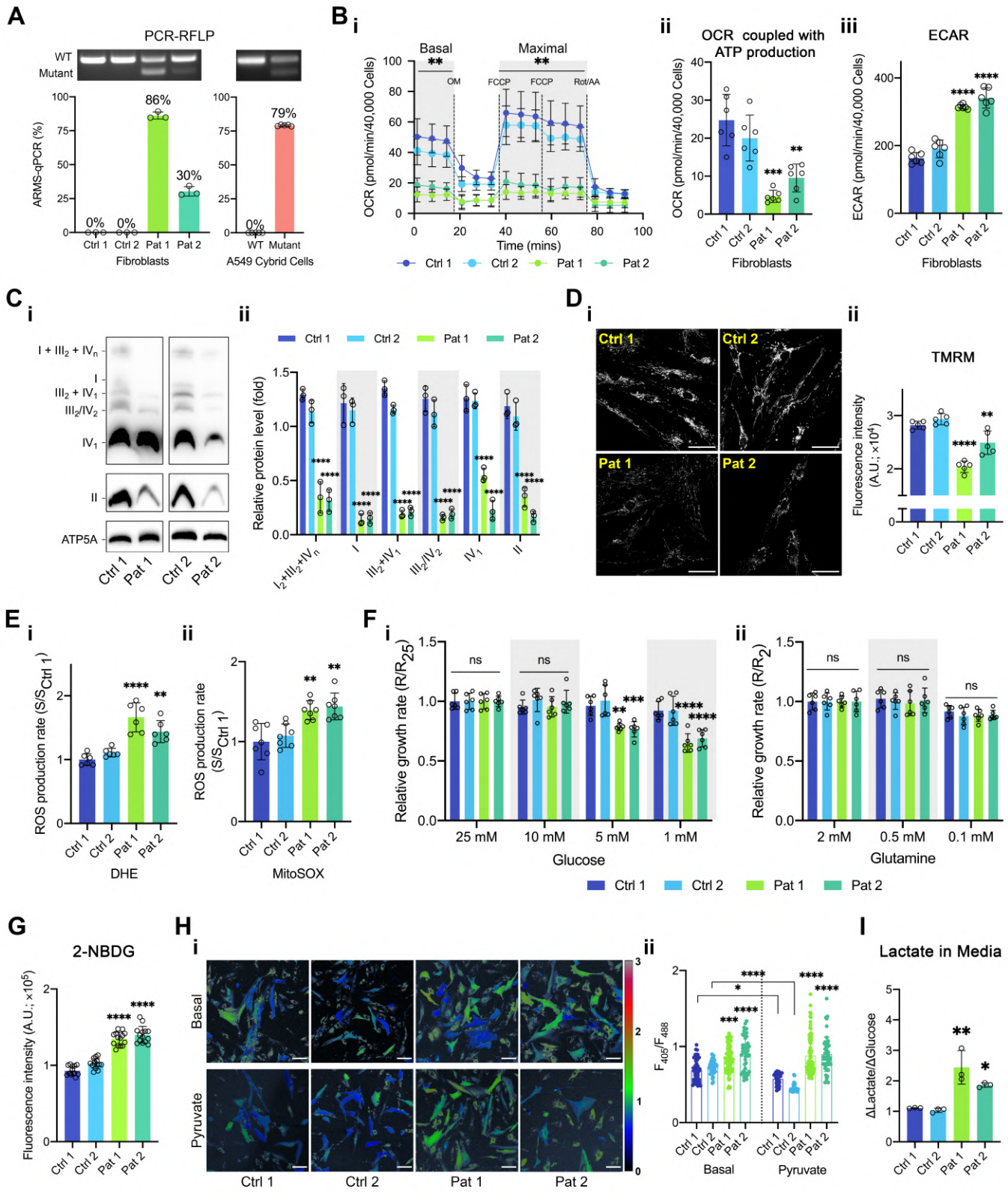
A
PCR-RFLP
WT
Mutant
ARMS-qPCR (%)
86%
30%
0%
0%
79%
0%
Ctrl 1
Ctrl 2
Pat 1
Pat 2
Fibroblasts
WT
Mutant
A549 Cybrid Cells
B i
Basal
Maximal
OM
FCCP
FCCP
Rot/AA
OCR (pmol/min/40,000 Cells)
Time (mins)
Ctrl 1
Ctrl 2
Pat 1
Pat 2
ii
OCR coupled with ATP production
Fibroblasts
iii
ECAR
ECAR (pmol/min/40,000 Cells)
Fibroblasts
C i
I + III2 + IVn
I
III2 + IV1
III2/IV2
IV1
II
ATP5A
Ctrl 1
Pat 1
Ctrl 2
Pat 2
ii
Relative protein level (fold)
I2+III2+IVn
I
III2+IV1
III2/IV2
IV1
II
D i
Ctrl 1
Ctrl 2
Pat 1
Pat 2
ii
TMRM
Fluorescence intensity (A.U.; ×10^4)
E i
ROS production rate (S/SCtrl 1)
DHE
ii
ROS production rate (S/SCtrl 1)
MitoSOX
F i
Relative growth rate (R/R25)
ns
25 mM
10 mM
5 mM
1 mM
Glucose
ii
Relative growth rate (R/R2)
2 mM
0.5 mM
0.1 mM
Glutamine
G
2-NBDG
Fluorescence intensity (A.U.; ×10^5)
H i
Basal
Pyruvate
Ctrl 1
Ctrl 2
Pat 1
Pat 2
ii
F405/F488
Basal
Pyruvate
I
Lactate in Media
ΔLactate/ΔGlucose

Fig. S1

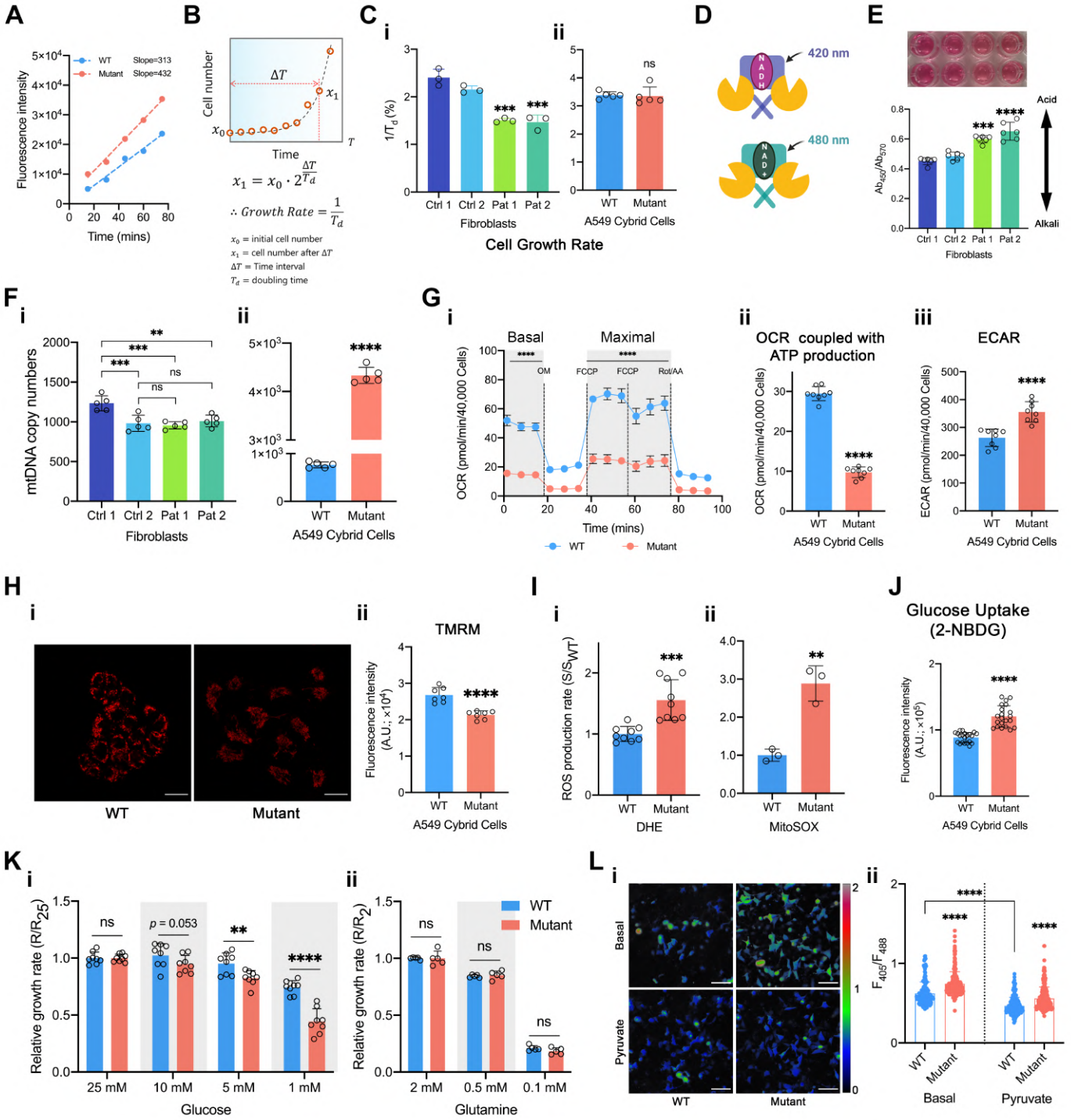
A
Fluorescence intensity
WT Slope=313
Mutant Slope=432
Time (mins)
B
Cell number
ΔT
Time
$x_1 = x_0 \cdot 2^{\frac{\Delta T}{T_d}}$
$\therefore Growth\ Rate = \frac{1}{T_d}$
x_0 = initial cell number
x_1 = cell number after ΔT
ΔT = Time interval
T_d = doubling time
C
i
1/T_d (%)
Ctrl 1 Ctrl 2 Pat 1 Pat 2
Fibroblasts
ii
ns
WT Mutant
A549 Cybrid Cells
Cell Growth Rate
D
420 nm
480 nm
E
Acid
Alkali
Ctrl 1 Ctrl 2 Pat 1 Pat 2
Fibroblasts
F
i
mtDNA copy numbers
Ctrl 1 Ctrl 2 Pat 1 Pat 2
Fibroblasts
ii
WT Mutant
A549 Cybrid Cells
G
i
Basal
Maximal
OM
FCCP
Rot/AA
OCR (pmol/min/40,000 Cells)
Time (mins)
WT Mutant
ii
OCR coupled with ATP production
iii
ECAR
H
i
WT
Mutant
ii
TMRM
Fluorescence intensity (A.U.; ×10⁴)
A549 Cybrid Cells
I
i
ROS production rate (S/S_WT)
DHE
ii
MitoSOX
J
Glucose Uptake (2-NBDG)
Fluorescence intensity (A.U.; ×10⁵)
A549 Cybrid Cells
K
i
Relative growth rate (R/R25)
ns
p = 0.053
25 mM 10 mM 5 mM 1 mM
Glucose
ii
Relative growth rate (R/R2)
WT Mutant
2 mM 0.5 mM 0.1 mM
Glutamine
L
i
Basal
Pyruvate
WT Mutant
ii
F405/F488
WT Mutant
Basal Pyruvate

Fig. 2

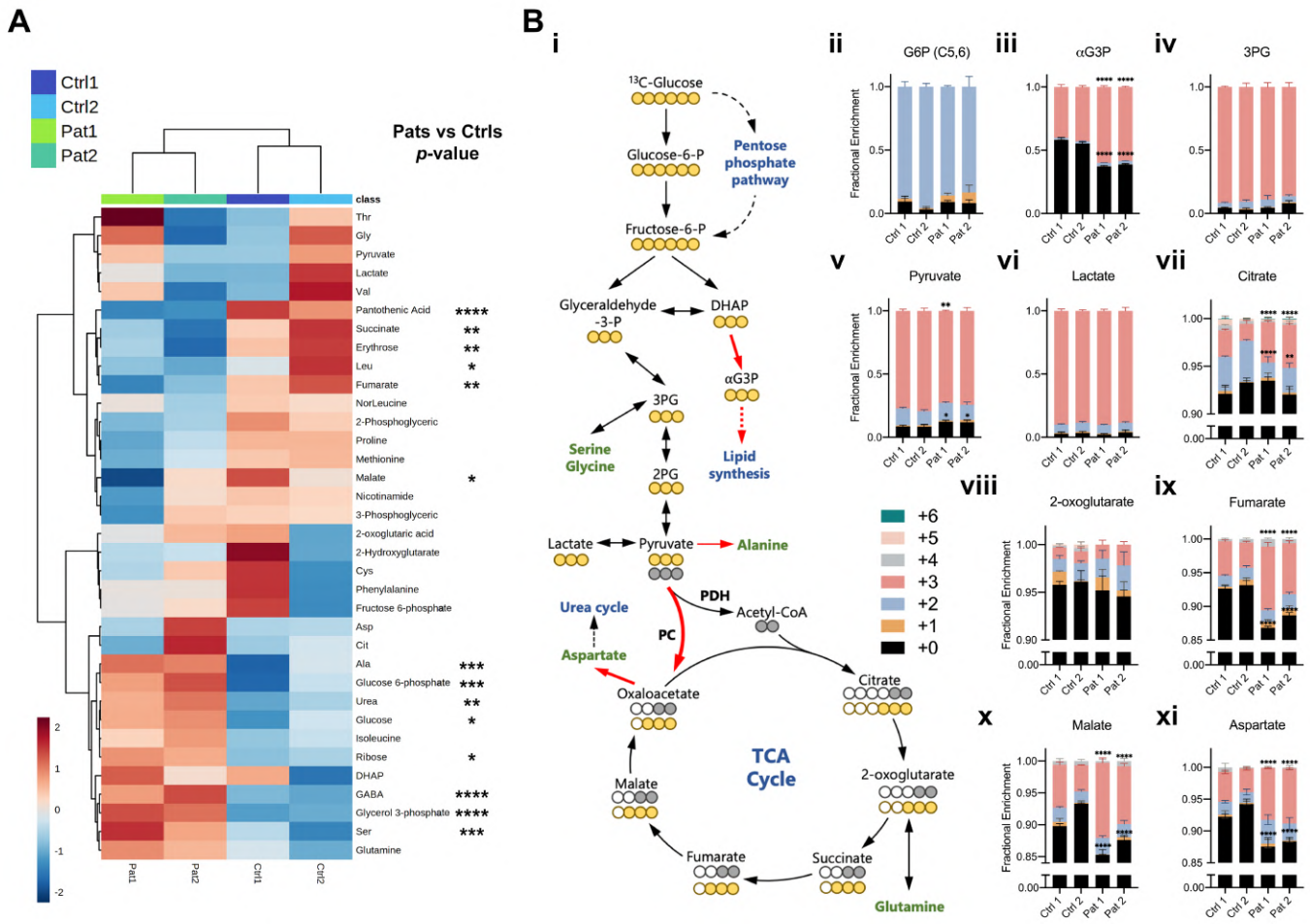
A
Ctrl1
Ctrl2
Pat1
Pat2
Pats vs Ctrls
p-value
class
Thr
Gly
Pyruvate
Lactate
Val
Pantothenic Acid ****
Succinate **
Erythrose **
Leu *
Fumarate **
NorLeucine
2-Phosphoglyceric
Proline
Methionine
Malate *
Nicotinamide
3-Phosphoglyceric
2-oxoglutaric acid
2-Hydroxyglutarate
Cys
Phenylalanine
Fructose 6-phosphate
Asp
Cit
Ala ***
Glucose 6-phosphate ***
Urea **
Glucose *
Isoleucine
Ribose *
DHAP
GABA ****
Glycerol 3-phosphate ****
Ser ***
Glutamine
Pat1
Pat2
Ctrl1
Ctrl2
B
i
13C-Glucose
Glucose-6-P
Pentose phosphate pathway
Fructose-6-P
Glyceraldehyde -3-P
DHAP
αG3P
3PG
Serine Glycine
2PG
Lipid synthesis
Lactate
Pyruvate
Alanine
PDH
Acetyl-CoA
Urea cycle
PC
Aspartate
Oxaloacetate
Citrate
TCA Cycle
Malate
2-oxoglutarate
Fumarate
Succinate
Glutamine
+6
+5
+4
+3
+2
+1
+0
ii
G6P (C5,6)
iii
αG3P
iv
3PG
v
Pyruvate
vi
Lactate
vii
Citrate
viii
2-oxoglutarate
ix
Fumarate
x
Malate
xi
Aspartate
Fractional Enrichment
Ctrl 1
Ctrl 2
Pat 1
Pat 2

Fig. S2

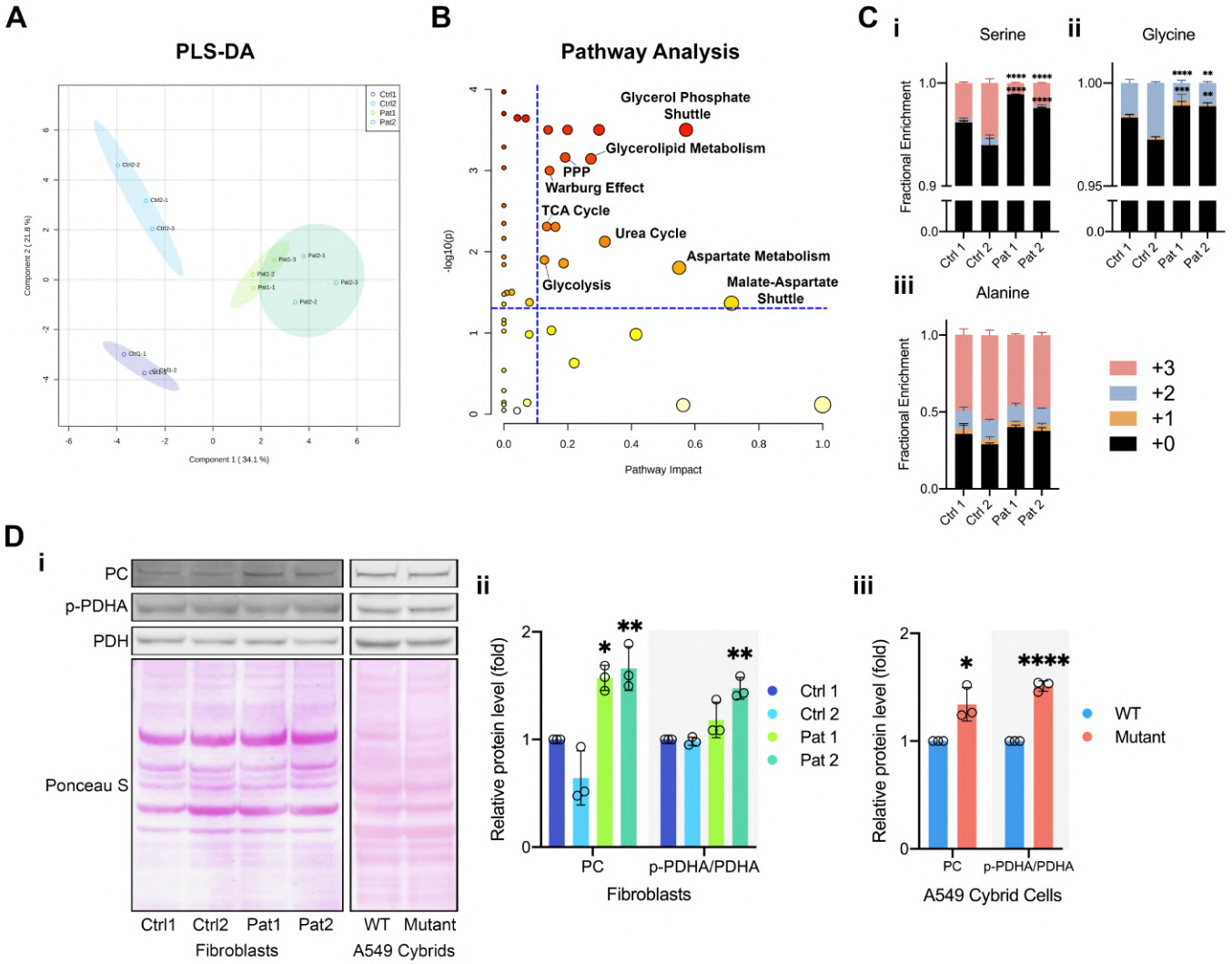
A
PLS-DA
Ctrl1
Ctrl2
Pat1
Pat2
Component 1 (34.1 %)
Component 2 (21.8 %)
B
Pathway Analysis
Glycerol Phosphate Shuttle
Glycerolipid Metabolism
PPP
Warburg Effect
TCA Cycle
Urea Cycle
Aspartate Metabolism
Glycolysis
Malate-Aspartate Shuttle
-log10(p)
Pathway Impact
C
i
Serine
ii
Glycine
iii
Alanine
Fractional Enrichment
Ctrl 1
Ctrl 2
Pat 1
Pat 2
+3
+2
+1
+0
D
i
PC
p-PDHA
PDH
Ponceau S
Ctrl1
Ctrl2
Pat1
Pat2
Fibroblasts
WT
Mutant
A549 Cybrids
ii
Relative protein level (fold)
PC
p-PDHA/PDHA
Fibroblasts
Ctrl 1
Ctrl 2
Pat 1
Pat 2
iii
Relative protein level (fold)
PC
p-PDHA/PDHA
A549 Cybrid Cells
WT
Mutant

Fig. 3

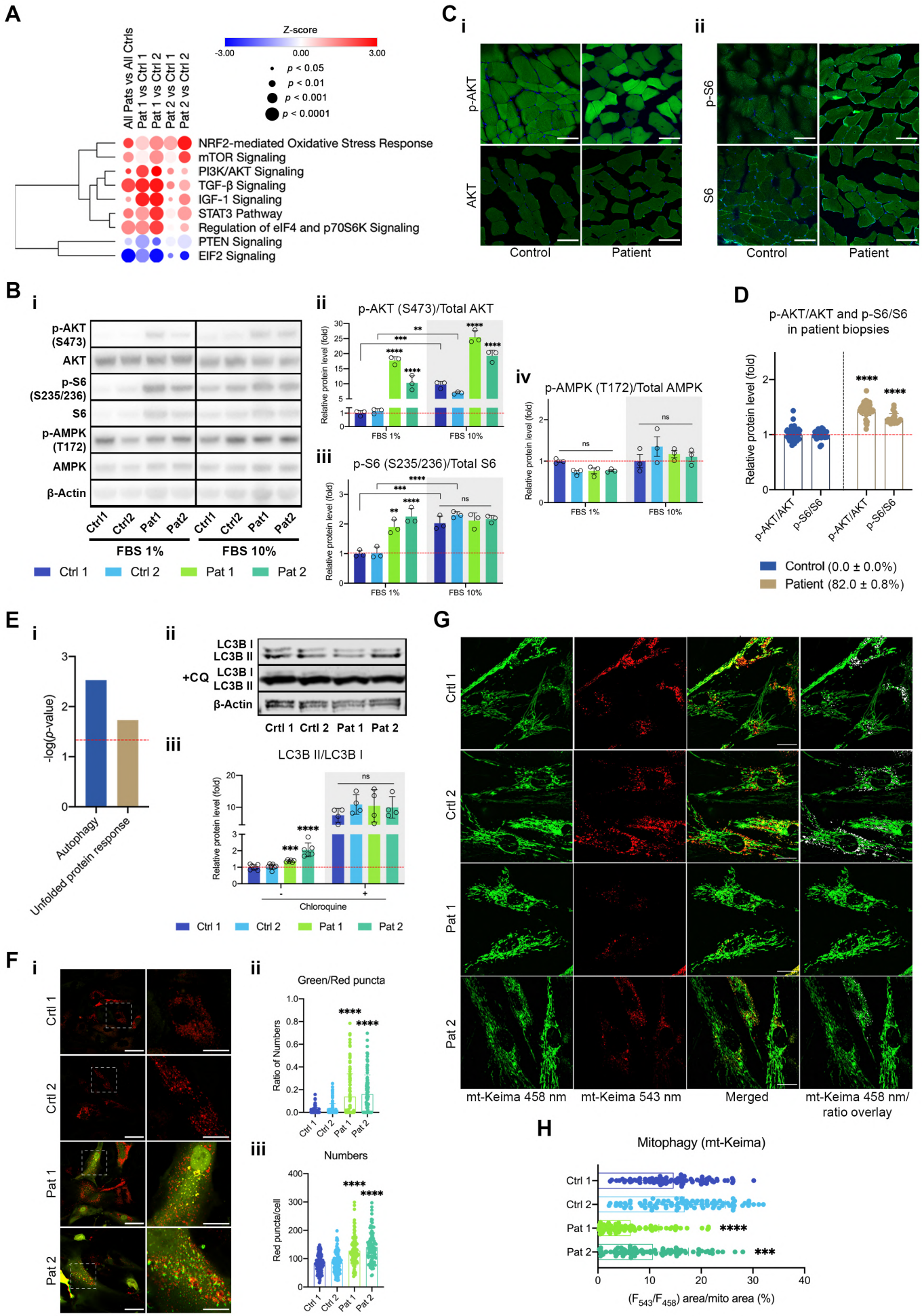
A
Z-score
-3.00
0.00
3.00
p < 0.05
p < 0.01
p < 0.001
p < 0.0001
All Pats vs All Ctrls
Pat 1 vs Ctrl 1
Pat 1 vs Ctrl 2
Pat 2 vs Ctrl 1
Pat 2 vs Ctrl 2
NRF2-mediated Oxidative Stress Response
mTOR Signaling
PI3K/AKT Signaling
TGF-β Signaling
IGF-1 Signaling
STAT3 Pathway
Regulation of eIF4 and p70S6K Signaling
PTEN Signaling
EIF2 Signaling
C
i
ii
p-AKT
AKT
p-S6
S6
Control
Patient
B
i
p-AKT (S473)
AKT
p-S6 (S235/236)
S6
p-AMPK (T172)
AMPK
β-Actin
Ctrl1
Ctrl2
Pat1
Pat2
FBS 1%
FBS 10%
Ctrl 1
Ctrl 2
Pat 1
Pat 2
ii
p-AKT (S473)/Total AKT
Relative protein level (fold)
iii
p-S6 (S235/236)/Total S6
iv
p-AMPK (T172)/Total AMPK
ns
D
p-AKT/AKT and p-S6/S6 in patient biopsies
Relative protein level (fold)
p-AKT/AKT
p-S6/S6
Control (0.0 ± 0.0%)
Patient (82.0 ± 0.8%)
E
i
-log(p-value)
Autophagy
Unfolded protein response
ii
LC3B I
LC3B II
+CQ
β-Actin
Crtl 1
Crtl 2
Pat 1
Pat 2
iii
LC3B II/LC3B I
Relative protein level (fold)
Chloroquine
G
Crtl 1
Crtl 2
Pat 1
Pat 2
mt-Keima 458 nm
mt-Keima 543 nm
Merged
mt-Keima 458 nm/ ratio overlay
F
i
ii
Green/Red puncta
Ratio of Numbers
iii
Numbers
Red puncta/cell
H
Mitophagy (mt-Keima)
(F543/F458) area/mito area (%)

Fig. S3

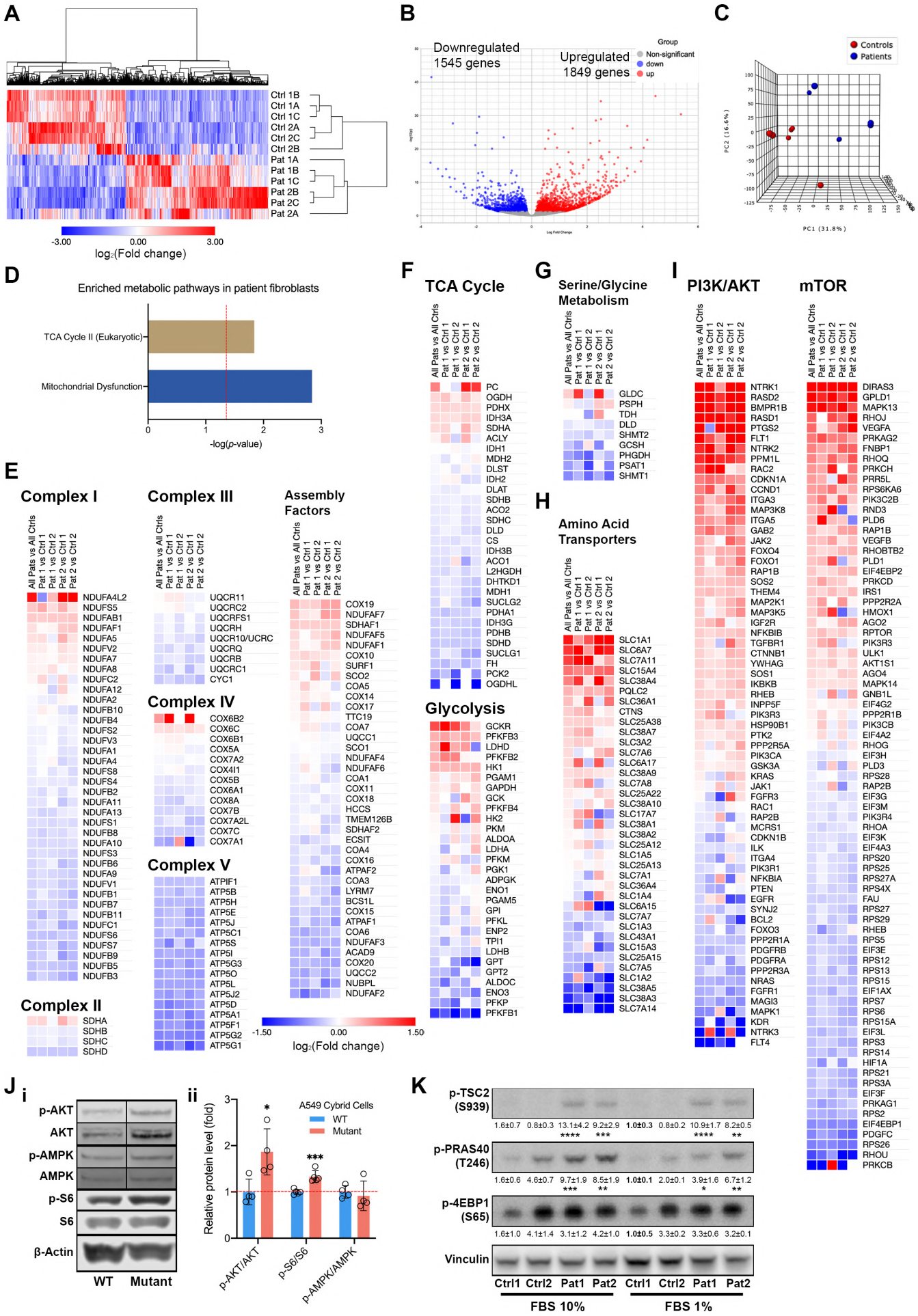
A
Ctrl 1B
Ctrl 1A
Ctrl 1C
Ctrl 2A
Ctrl 2C
Ctrl 2B
Pat 1A
Pat 1B
Pat 1C
Pat 2B
Pat 2C
Pat 2A
-3.00
0.00
3.00
log2(Fold change)
B
Downregulated
1545 genes
Upregulated
1849 genes
Group
Non-significant
down
up
C
Controls
Patients
PC1 (31.8%)
PC2 (16.6%)
D
Enriched metabolic pathways in patient fibroblasts
TCA Cycle II (Eukaryotic)
Mitochondrial Dysfunction
-log(p-value)
E
Complex I
Complex III
Assembly Factors
Complex IV
Complex V
Complex II
All Pats vs All Ctrls
Pat 1 vs Ctrl 1
Pat 1 vs Ctrl 2
Pat 2 vs Ctrl 1
Pat 2 vs Ctrl 2
NDUFA4L2
NDUFS5
NDUFAB1
NDUFAF1
NDUFA5
NDUFV2
NDUFA7
NDUFA8
NDUFC2
NDUFA12
NDUFA2
NDUFB10
NDUFB4
NDUFS2
NDUFV3
NDUFA1
NDUFA4
NDUFS8
NDUFS4
NDUFB2
NDUFA11
NDUFA13
NDUFS1
NDUFB8
NDUFA10
NDUFS3
NDUFB6
NDUFA9
NDUFV1
NDUFB1
NDUFB7
NDUFB11
NDUFC1
NDUFS6
NDUFS7
NDUFB9
NDUFB5
NDUFB3
UQCR11
UQCRC2
UQCRFS1
UQCRH
UQCR10/UCRC
UQCRQ
UQCRB
UQCRC1
CYC1
COX6B2
COX6C
COX6B1
COX5A
COX7A2
COX4I1
COX5B
COX6A1
COX8A
COX7B
COX7A2L
COX7C
COX7A1
ATPIF1
ATP5B
ATP5H
ATP5E
ATP5J
ATP5C1
ATP5S
ATP5I
ATP5G3
ATP5O
ATP5L
ATP5J2
ATP5D
ATP5A1
ATP5F1
ATP5G2
ATP5G1
SDHA
SDHB
SDHC
SDHD
COX19
NDUFAF7
SDHAF1
NDUFAF5
NDUFAF1
COX10
SURF1
SCO2
COA5
COX14
COX17
TTC19
COA7
UQCC1
SCO1
NDUFAF4
NDUFAF6
COA1
COX11
COX18
HCCS
TMEM126B
SDHAF2
ECSIT
COA4
COX16
ATPAF2
COA3
LYRM7
BCS1L
COX15
ATPAF1
COA6
NDUFAF3
ACAD9
COX20
UQCC2
NUBPL
NDUFAF2
-1.50
0.00
1.50
log2(Fold change)
F
TCA Cycle
PC
OGDH
PDHX
IDH3A
SDHA
ACLY
IDH1
MDH2
DLST
IDH2
DLAT
SDHB
ACO2
SDHC
DLD
CS
IDH3B
ACO1
L2HGDH
DHTKD1
MDH1
SUCLG2
PDHA1
IDH3G
PDHB
SDHD
SUCLG1
FH
PCK2
OGDHL
Glycolysis
GCKR
PFKFB3
LDHD
PFKFB2
HK1
PGAM1
GAPDH
GCK
PFKFB4
HK2
PKM
ALDOA
LDHA
PFKM
PGK1
ADPGK
ENO1
PGAM5
GPI
PFKL
ENP2
TPI1
LDHB
GPT
GPT2
ALDOC
ENO3
PFKP
PFKFB1
G
Serine/Glycine Metabolism
GLDC
PSPH
TDH
DLD
SHMT2
GCSH
PHGDH
PSAT1
SHMT1
H
Amino Acid Transporters
SLC1A1
SLC6A7
SLC7A11
SLC15A4
SLC38A4
PQLC2
SLC36A1
CTNS
SLC25A38
SLC38A7
SLC3A2
SLC7A6
SLC6A17
SLC38A9
SLC7A8
SLC25A22
SLC38A10
SLC17A7
SLC38A1
SLC38A2
SLC25A12
SLC1A5
SLC25A13
SLC7A1
SLC36A4
SLC1A4
SLC6A15
SLC7A7
SLC1A3
SLC43A1
SLC15A3
SLC25A15
SLC7A5
SLC1A2
SLC38A5
SLC38A3
SLC7A14
I
PI3K/AKT
mTOR
NTRK1
RASD2
BMPR1B
RASD1
PTGS2
FLT1
NTRK2
PPM1L
RAC2
CDKN1A
CCND1
ITGA3
MAP3K8
ITGA5
GAB2
JAK2
FOXO4
FOXO1
RAP1B
SOS2
THEM4
MAP2K1
MAP3K5
IGF2R
NFKBIB
TGFBR1
CTNNB1
YWHAG
SOS1
IKBKB
RHEB
INPP5F
PIK3R3
HSP90B1
PTK2
PPP2R5A
PIK3CA
GSK3A
KRAS
JAK1
FGFR3
RAC1
RAP2B
MCRS1
CDKN1B
ILK
ITGA4
PIK3R1
NFKBIA
PTEN
EGFR
SYNJ2
BCL2
FOXO3
PPP2R1A
PDGFRB
PDGFRA
PPP2R3A
NRAS
FGFR1
MAGI3
MAPK1
KDR
NTRK3
FLT4
DIRAS3
GPLD1
MAPK13
RHOJ
VEGFA
PRKAG2
FNBP1
RHOQ
PRKCH
PRR5L
RPS6KA6
PIK3C2B
RND3
PLD6
RAP1B
VEGFB
RHOBTB2
PLD1
EIF4EBP2
PRKCD
IRS1
PPP2R2A
HMOX1
AGO2
RPTOR
PIK3R3
ULK1
AKT1S1
AGO4
MAPK14
GNB1L
EIF4G2
PPP2R1B
PIK3CB
EIF4A2
RHOG
EIF3H
PLD3
RPS28
RAP2B
EIF3G
EIF3M
PIK3R4
RHOA
EIF3K
EIF4A3
RPS20
RPS25
RPS27A
RPS4X
FAU
RPS27
RPS29
RHEB
RPS5
EIF3E
RPS12
RPS13
RPS15
EIF1AX
RPS7
RPS6
RPS15A
EIF3L
RPS3
RPS14
HIF1A
RPS21
RPS3A
EIF3F
PRKAG1
RPS2
EIF4EBP1
PDGFC
RPS26
RHOU
PRKCB
J
i
p-AKT
AKT
p-AMPK
AMPK
p-S6
S6
β-Actin
WT
Mutant
ii
A549 Cybrid Cells
WT
Mutant
Relative protein level (fold)
p-AKT/AKT
p-S6/S6
p-AMPK/AMPK
K
p-TSC2 (S939)
1.6±0.7 0.8±0.3 13.1±4.2 9.2±2.9 1.0±0.3 0.8±0.2 10.9±1.7 8.2±0.5
p-PRAS40 (T246)
1.6±0.6 4.6±0.7 9.7±1.9 8.5±1.9 1.0±0.1 2.0±0.1 3.9±1.6 6.7±1.2
p-4EBP1 (S65)
1.6±1.0 4.1±1.4 3.1±1.2 4.2±1.0 1.0±0.5 3.3±0.2 3.3±0.6 3.2±0.1
Vinculin
Ctrl1 Ctrl2 Pat1 Pat2 Ctrl1 Ctrl2 Pat1 Pat2
FBS 10%
FBS 1%

Fig. S4

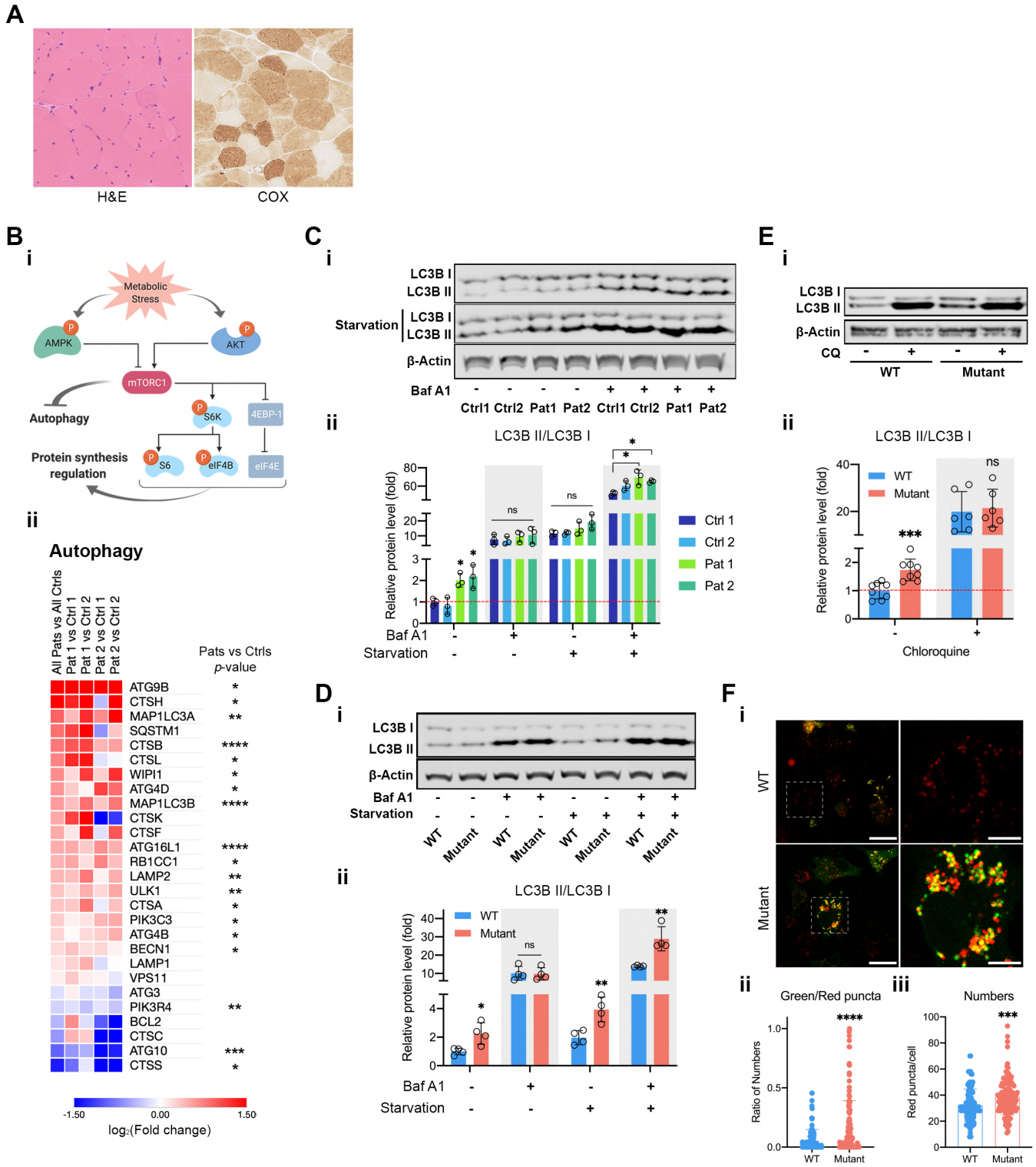
A
H&E
COX
B
i
Metabolic Stress
AMPK
AKT
mTORC1
Autophagy
S6K
4EBP-1
Protein synthesis regulation
S6
eIF4B
eIF4E
ii
Autophagy
All Pats vs All Ctrls
Pat 1 vs Ctrl 1
Pat 1 vs Ctrl 2
Pat 2 vs Ctrl 1
Pat 2 vs Ctrl 2
Pats vs Ctrls p-value
ATG9B *
CTSH *
MAP1LC3A **
SQSTM1
CTSB ****
CTSL *
WIPI1 *
ATG4D *
MAP1LC3B ****
CTSK
CTSF
ATG16L1 ****
RB1CC1 *
LAMP2 **
ULK1 **
CTSA *
PIK3C3 *
ATG4B *
BECN1 *
LAMP1
VPS11
ATG3
PIK3R4 **
BCL2
CTSC
ATG10 ***
CTSS *
-1.50
0.00
1.50
log2(Fold change)
C
i
LC3B I
LC3B II
Starvation
β-Actin
Baf A1
Ctrl1 Ctrl2 Pat1 Pat2 Ctrl1 Ctrl2 Pat1 Pat2
ii
LC3B II/LC3B I
Relative protein level (fold)
ns
Ctrl 1
Ctrl 2
Pat 1
Pat 2
Baf A1
Starvation
D
i
LC3B I
LC3B II
β-Actin
Baf A1
Starvation
WT Mutant WT Mutant WT Mutant WT Mutant
ii
LC3B II/LC3B I
Relative protein level (fold)
WT
Mutant
ns
Baf A1
Starvation
E
i
LC3B I
LC3B II
β-Actin
CQ
WT
Mutant
ii
LC3B II/LC3B I
Relative protein level (fold)
WT
Mutant
ns
Chloroquine
F
i
WT
Mutant
ii
Green/Red puncta
Ratio of Numbers
WT
Mutant
iii
Numbers
Red puncta/cell
WT
Mutant
G
The COX8-mCherry-EGFP reporter (mitophagy)
Vehicle
Oligo+AA
Oligo+AA+Baf A1
A549 WT cells
A549 Cybrids
mCherry
EGFP

Tables S1-4

Table S1. Upstream analysis for Kinase in patient fibroblasts by IPA.

Kinase	Prediction	Z-score	*p*-value
CDKN1A	Activated	3.084	1.12E-08
IKBKB		3.244	0.000377
AKT1		2.47	0.00201
MAPK13		2.079	0.00245
TGFBR2		2.747	0.00255
PTK2		2.48	0.00302
CHUK		4.427	0.00929
STK11	Inhibited	-2.494	0.00000766
INSR		-2.032	0.000675
CCNK		-2.399	0.000866
AURKB		-2.772	0.005

Table S2. Upstream analysis for translation regulator in patient fibroblasts by IPA.

Translation regulator	Prediction	Z-score	*p*-value
EIF4E	Inhibited	-2.169	0.000541
EIF4G1		-2.333	0.00245

Table S3. Upstream analysis for transcription regulators in patient fibroblasts by IPA.

Transcription regulator	Prediction	Z-score	*p*-value
TP53	Activated	3.282	2.79E-21
NUPR1		4.066	5.29E-11
KDM5B		3.627	0.00000101
CTNNB1		2.96	0.00000321
NFKBIA		2.632	0.0000157
GLI1		2.971	0.0000256
TCF4		2.225	0.0000457
SMARCA4		3.609	0.000108
KLF4		2.946	0.000627
PTTG1		2.302	0.000791
TFEB		3.273	0.0008
CDKN2A		4.62	0.000838
TCF7L2		4.059	0.000841
TCF3		3.926	0.00118
HIF1A		2.117	0.00224
CREB1		3.164	0.00238
HDAC1		2.228	0.00248
RBCK1		2.236	0.00252
E2F6		2.53	0.00259
ATF4		2.495	0.00296
SMARCD3		2.813	0.005
HDAC2		2.468	0.00621
ERG		2.557	0.00988
EP300		2.298	0.00994
TBX2	Inhibited	-4.488	2.43E-08
MYC		-4.01	2.46E-07
MYCN		-5.406	0.00000442
GMNN		-2.746	0.0000098
SOX1		-3	0.0000215
HOXA9		-2.01	0.0000273
E2F3		-3.186	0.0000273
SOX3		-3	0.00012
RUNX3		-2.272	0.000213

Table S4. Upstream analysis using published RNA-seq dataset of patient biopsies by IPA.

Upstream Regulator	Molecule Type	*p*-value
TRIB3	Kinase	0.0000295
MTOR		0.00112
TGFBR2		0.0101
GNE		0.0155
PIK3R1		0.0159
TGFBR1		0.0166
CDK19		0.0199
Growth hormone	Group	0.000165
Foxo		0.000504
ADRB		0.00393
Insulin		0.00402
YAP/TAZ		0.0089
Pro-inflammatory Cytokine		0.0101
PI3K (family)		0.026
Rxr		0.0269
ATF4	Transcription Regulator	0.00048
MLX		0.000905
PPARGC1A		0.00115
EP300		0.0029
FOXO1		0.00299
MLXIPL		0.00326
MLXIP		0.00446
ZNF282		0.0089
MYRF		0.0104
HDAC5		0.0122
NKX2-3		0.0127
MYC		0.0131
STAT6		0.0149
ZNF100		0.0155
ZNF85		0.0155
ZNF254		0.0155
ZNF431		0.0155
ZNF43		0.0155
ZNF429		0.0155
HDAC10		0.0177
ZNF91		0.0177
ATF5		0.0221
PA2G4		0.0221
KAT5		0.0231
STAT5B		0.026
AJUBA		0.0265
DDIT3		0.0282
BHLHE41		0.0287
ARNT		0.0304
PIAS4		0.0308
THRAP3		0.033
PLAGL1		0.033
KLF11		0.0337
CREBZF		0.0352
CBX4		0.0352
TCF7L2		0.0374
MNT		0.0416
ACTN4		0.0416
CREB3L3		0.0438
NONO		0.0438
MED12		0.0459
SIN3B		0.0459
PBX3		0.048
HNF4A		0.048
MED1		0.0492

Fig. 4

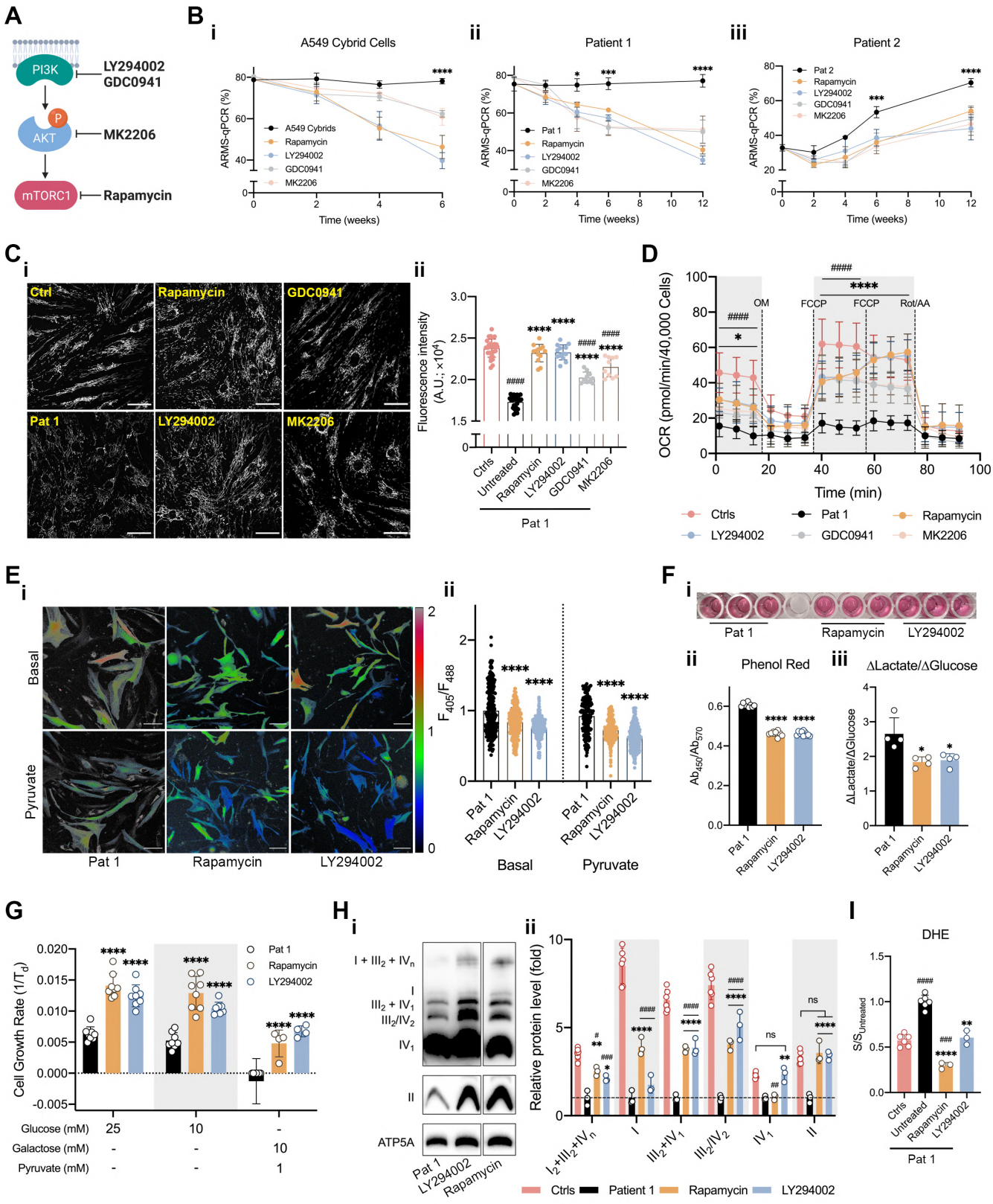
A
PI3K
LY294002
GDC0941
P
AKT
MK2206
mTORC1
Rapamycin
B
i
A549 Cybrid Cells
ARMS-qPCR (%)
Time (weeks)
A549 Cybrids
Rapamycin
LY294002
GDC0941
MK2206
ii
Patient 1
iii
Patient 2
Pat 2
C
i
Ctrl
Rapamycin
GDC0941
Pat 1
LY294002
MK2206
ii
Fluorescence intensity (A.U.; ×10⁴)
Ctrls
Untreated
Rapamycin
LY294002
GDC0941
MK2206
Pat 1
D
OCR (pmol/min/40,000 Cells)
OM
FCCP
FCCP
Rot/AA
Time (min)
Ctrls
Pat 1
Rapamycin
LY294002
GDC0941
MK2206
E
i
Basal
Pyruvate
Pat 1
Rapamycin
LY294002
ii
F405/F488
Basal
Pyruvate
F
i
Pat 1
Rapamycin
LY294002
ii
Phenol Red
Ab450/Ab570
iii
ΔLactate/ΔGlucose
G
Cell Growth Rate (1/Td)
Pat 1
Rapamycin
LY294002
Glucose (mM)
Galactose (mM)
Pyruvate (mM)
H
i
I + III2 + IVn
I
III2 + IV1
III2/IV2
IV1
II
ATP5A
Pat 1
LY294002
Rapamycin
ii
Relative protein level (fold)
Ctrls
Patient 1
Rapamycin
LY294002
I
DHE
S/SUntreated
Ctrls
Untreated
Rapamycin
LY294002
Pat 1

Fig. S5

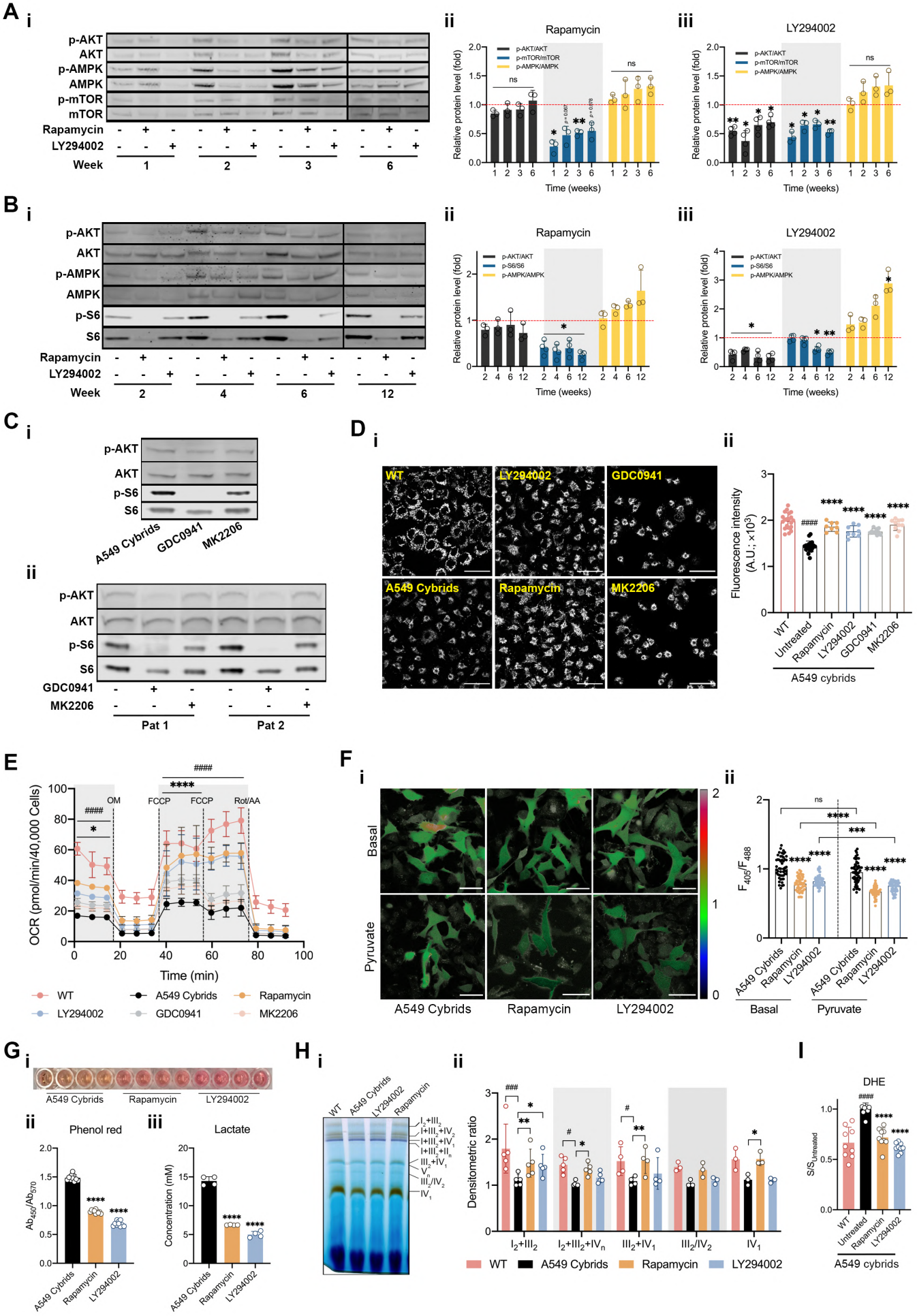
A
i
p-AKT
AKT
p-AMPK
AMPK
p-mTOR
mTOR
Rapamycin
LY294002
Week
ii
Rapamycin
iii
LY294002
Relative protein level (fold)
Time (weeks)
B
p-S6
S6
C
A549 Cybrids
GDC0941
MK2206
Pat 1
Pat 2
D
WT
Untreated
Fluorescence intensity (A.U.; ×10³)
E
OCR (pmol/min/40,000 Cells)
Time (min)
OM
FCCP
Rot/AA
F
Basal
Pyruvate
G
Phenol red
Lactate
Concentration (mM)
H
Densitometric ratio
I
DHE

Fig. 5

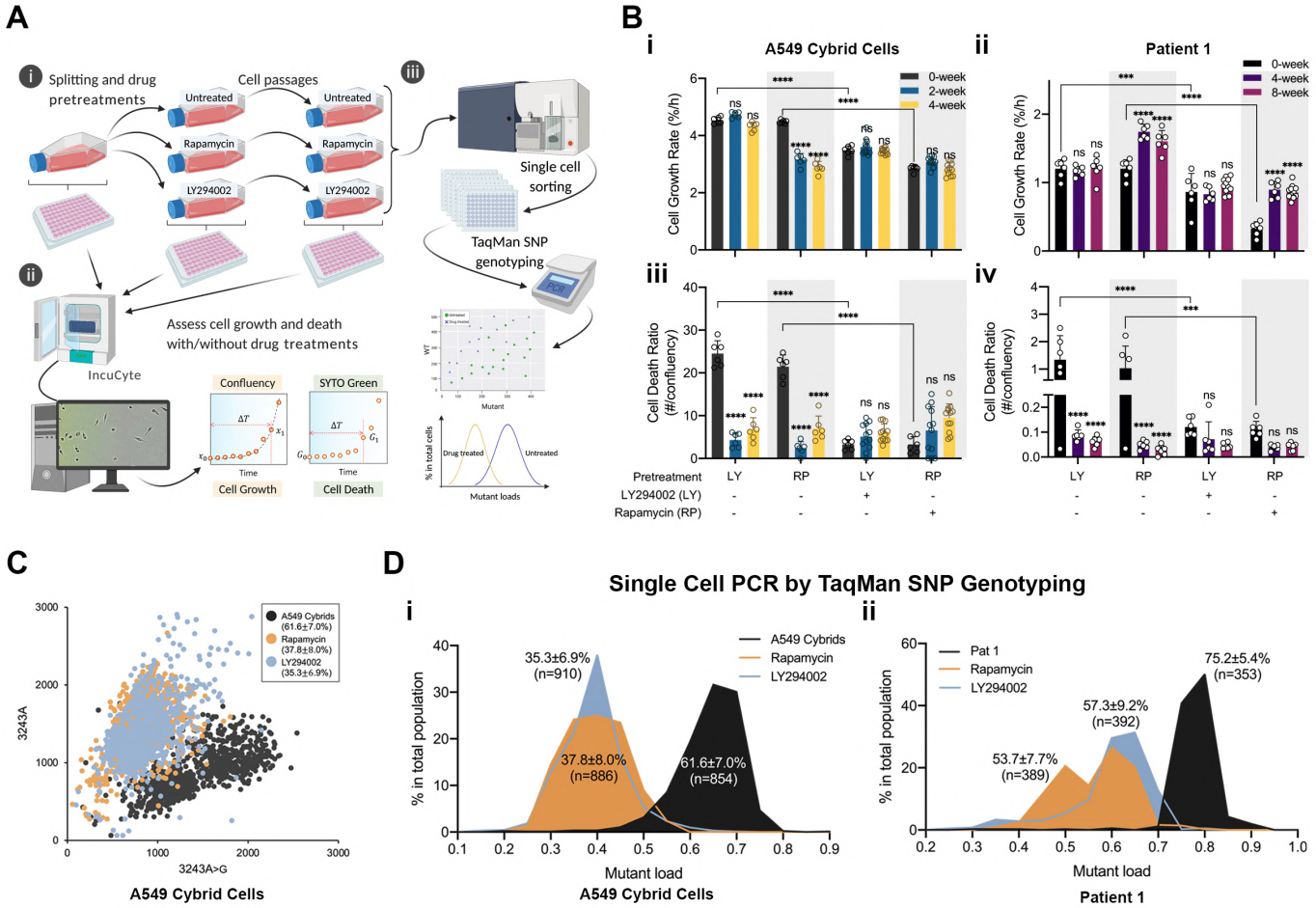
A
i Splitting and drug pretreatments
Cell passages
Untreated
Rapamycin
LY294002
iii
Single cell sorting
TaqMan SNP genotyping
ii
Assess cell growth and death with/without drug treatments
IncuCyte
Confluency
SYTO Green
Time
Cell Growth
Cell Death
Mutant
Mutant loads
Drug treated
Untreated
B
i
A549 Cybrid Cells
ii
Patient 1
0-week
2-week
4-week
8-week
Cell Growth Rate (%/h)
iii
iv
Cell Death Ratio (#/confluency)
Pretreatment
LY294002 (LY)
Rapamycin (RP)
LY
RP

C
A549 Cybrids (61.6±7.0%)
Rapamycin (37.8±8.0%)
LY294002 (35.3±6.9%)
3243A
3243A>G
A549 Cybrid Cells
D
Single Cell PCR by TaqMan SNP Genotyping
i
A549 Cybrids
Rapamycin
LY294002
35.3±6.9% (n=910)
37.8±8.0% (n=886)
61.6±7.0% (n=854)
% in total population
Mutant load
A549 Cybrid Cells
ii
Pat 1
Rapamycin
LY294002
75.2±5.4% (n=353)
57.3±9.2% (n=392)
53.7±7.7% (n=389)
Patient 1

Fig. S6

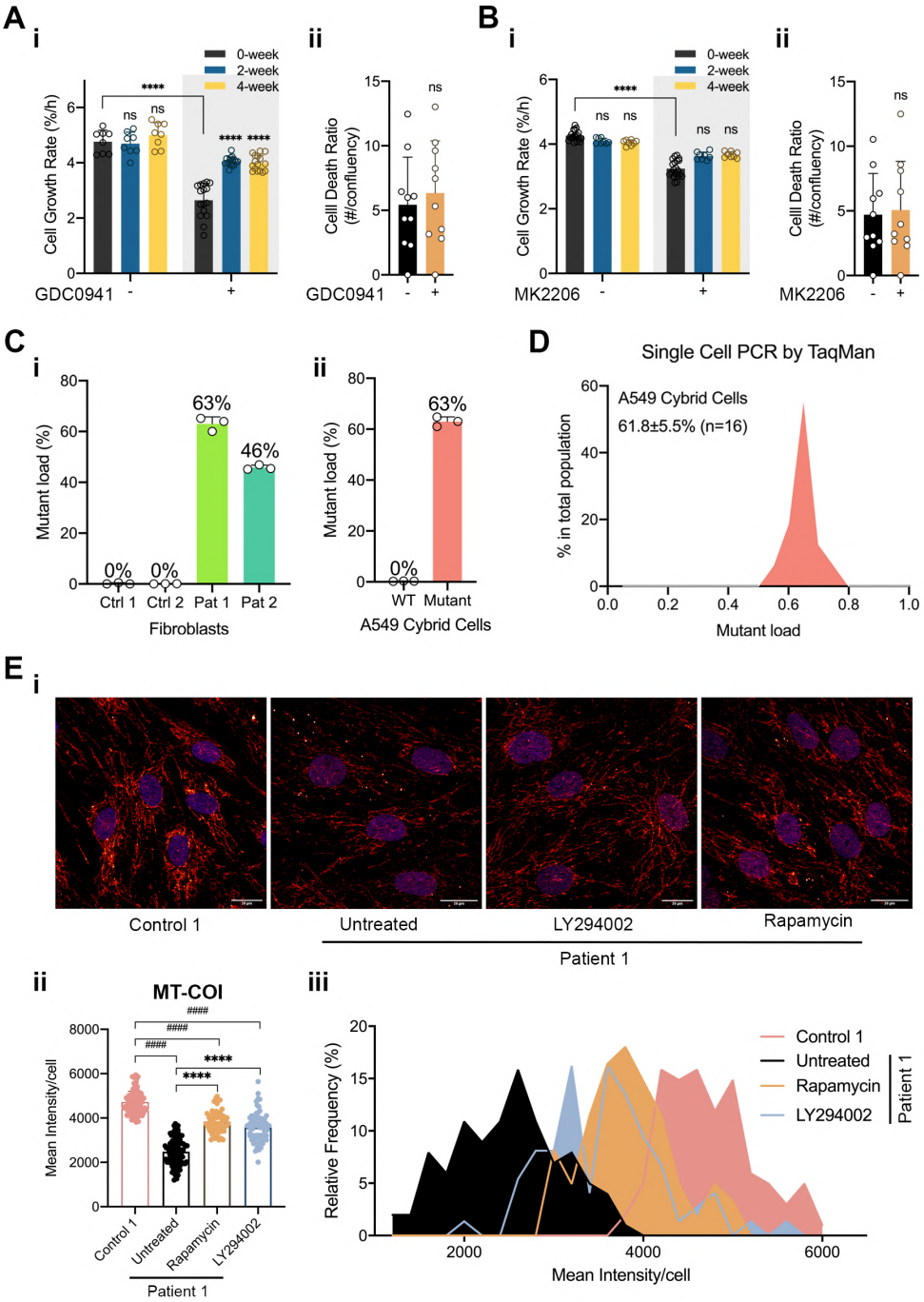
A
i
0-week
2-week
4-week
Cell Growth Rate (%/h)
GDC0941
ii
Celll Death Ratio (#/confluency)
B
MK2206
C
Mutant load (%)
63%
46%
0%
Ctrl 1
Ctrl 2
Pat 1
Pat 2
Fibroblasts
WT
Mutant
A549 Cybrid Cells
D
Single Cell PCR by TaqMan
A549 Cybrid Cells
61.8±5.5% (n=16)
% in total population
Mutant load
E
Control 1
Untreated
LY294002
Rapamycin
Patient 1
MT-COI
Mean Intensity/cell
Relative Frequency (%)

Fig. 6

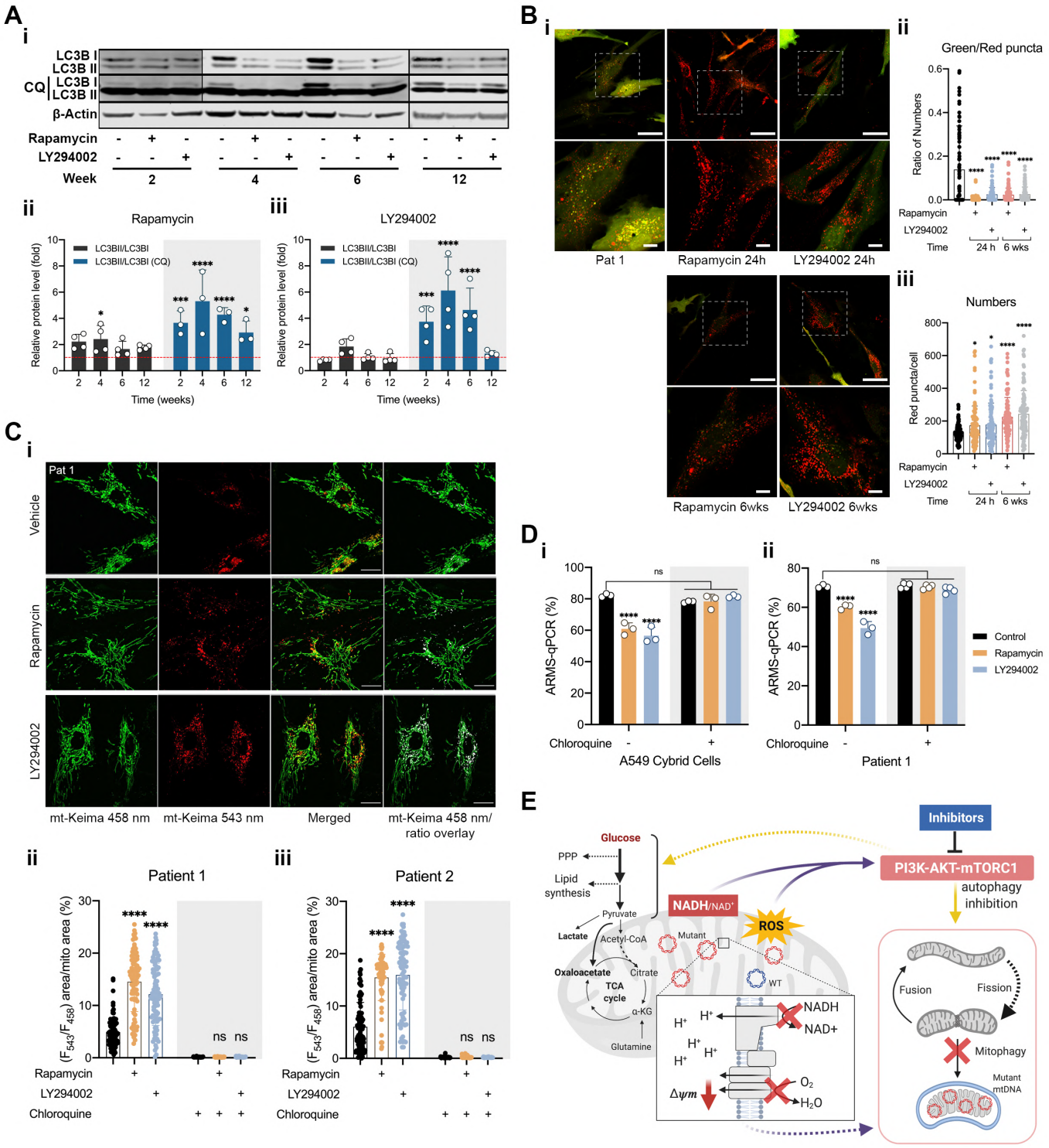
A
i
LC3B I
LC3B II
CQ
LC3B I
LC3B II
β-Actin
Rapamycin
LY294002
Week
2
4
6
12
ii
Rapamycin
iii
LY294002
LC3BII/LC3BI
LC3BII/LC3BI (CQ)
Relative protein level (fold)
Time (weeks)
B
i
Pat 1
Rapamycin 24h
LY294002 24h
Rapamycin 6wks
LY294002 6wks
ii
Green/Red puncta
Ratio of Numbers
Rapamycin
LY294002
Time
24 h
6 wks
iii
Numbers
Red puncta/cell
C
i
Pat 1
Vehicle
Rapamycin
LY294002
mt-Keima 458 nm
mt-Keima 543 nm
Merged
mt-Keima 458 nm/ ratio overlay
ii
Patient 1
iii
Patient 2
(F543/F458) area/mito area (%)
Rapamycin
LY294002
Chloroquine
ns
D
i
ii
ARMS-qPCR (%)
Chloroquine
A549 Cybrid Cells
Patient 1
Control
Rapamycin
LY294002
E
Glucose
PPP
Lipid synthesis
Pyruvate
Lactate
Acetyl-CoA
Oxaloacetate
Citrate
TCA cycle
α-KG
Glutamine
NADH/NAD+
ROS
Mutant
WT
NADH
NAD+
O2
H2O
Δψm
Inhibitors
PI3K-AKT-mTORC1
autophagy inhibition
Fusion
Fission
Mitophagy
Mutant mtDNA

Fig. S7

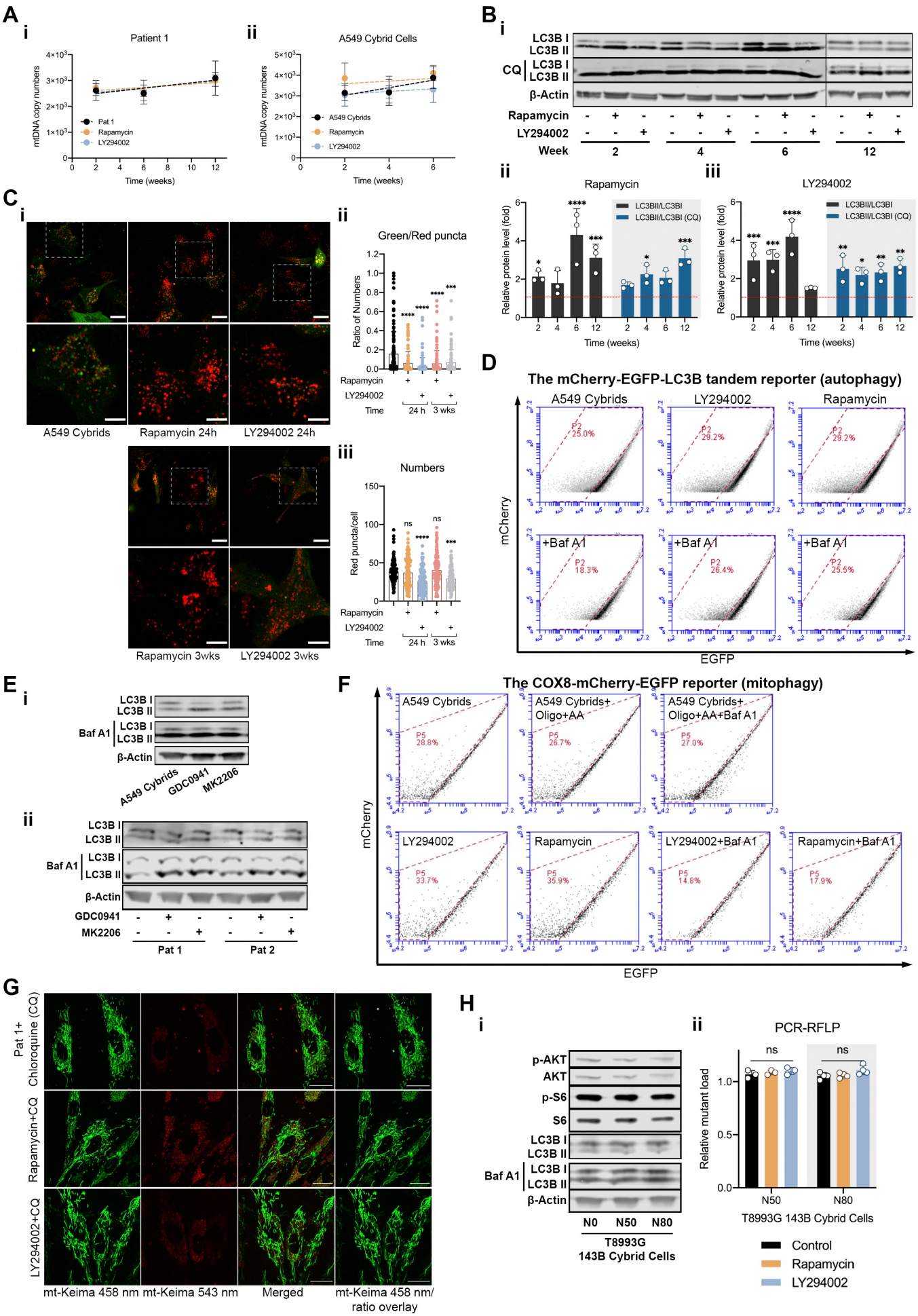
A
i
Patient 1
mtDNA copy numbers
Pat 1
Rapamycin
LY294002
Time (weeks)
ii
A549 Cybrid Cells
A549 Cybrids
Rapamycin
LY294002
B
i
LC3B I
LC3B II
CQ
β-Actin
Rapamycin
LY294002
Week
ii
Rapamycin
iii
LY294002
Relative protein level (fold)
LC3BII/LC3BI
LC3BII/LC3BI (CQ)
Time (weeks)
C
i
A549 Cybrids
Rapamycin 24h
LY294002 24h
Rapamycin 3wks
LY294002 3wks
ii
Green/Red puncta
Ratio of Numbers
24 h
3 wks
iii
Numbers
Red puncta/cell
D
The mCherry-EGFP-LC3B tandem reporter (autophagy)
A549 Cybrids
LY294002
Rapamycin
+Baf A1
mCherry
EGFP
E
i
Baf A1
A549 Cybrids
GDC0941
MK2206
ii
Pat 1
Pat 2
F
The COX8-mCherry-EGFP reporter (mitophagy)
A549 Cybrids
A549 Cybrids+ Oligo+AA
A549 Cybrids+ Oligo+AA+Baf A1
LY294002
Rapamycin
LY294002+Baf A1
Rapamycin+Baf A1
G
Pat 1+ Chloroquine (CQ)
Rapamycin+CQ
LY294002+CQ
mt-Keima 458 nm
mt-Keima 543 nm
Merged
mt-Keima 458 nm/ ratio overlay
H
i
p-AKT
AKT
p-S6
S6
N0
N50
N80
T8993G
143B Cybrid Cells
ii
PCR-RFLP
Relative mutant load
ns
Control
Rapamycin
LY294002